HIGHER-ORDER DGFEM TRANSPORT CALCULATIONS ON POLYTOPE MESHES FOR MASSIVELY-PARALLEL ARCHITECTURES

A Dissertation

by

MICHAEL WAYNE HACKEMACK

Submitted to the Office of Graduate and Professional Studies of
Texas A&M University
in partial fulfillment of the requirements for the degree of

DOCTOR OF PHILOSOPHY

Chair of Committee,	Jean Ragusa
Committee Members,	Marvin Adams
	Jim Morel
	Nancy Amato
	Troy Becker
Head of Department,	Yassin Hassan

May 2016

Major Subject: Nuclear Engineering

TABLE OF CONTENTS

Page

LIST OF FIGURES

FIGURE Page

LIST OF TABLES

TABLE Page

1. INTRODUCTION

1.1 Current State of the Problem

1.2 Purpose of the Dissertation

1.3 Organization of the Dissertation

In this introductory chapter, we have presented a summary of work performed. We also gave our motivation for choosing this work as well as a brief discussion of previous work that has directly influenced this dissertation. We conclude this intoduction by briefly describing the remaining chapters of this dissertation.

2. THE DGFEM FORMULATION OF THE MULTIGROUP S_N EQUATIONS

The movement of bulk materials and particles through some medium can be described with the statistical behavior of a non-equilibrium system. Boltzmann first devised these probabilistic field equations to characterize fluid flow via driving temperature gradients [1]. His work was later extended to model general fluid flow, heat conduction, hamiltonian mechanics, quantum theory, general relativity, and radiation transport, among others. The Boltzmann Equation can be written in the general form:

$$\frac{\partial u}{\partial t} = \left(\frac{\partial u}{\partial t}\right)_{force} + \left(\frac{\partial u}{\partial t}\right)_{advec} + \left(\frac{\partial u}{\partial t}\right)_{coll} \tag{2.1}$$

where $u(\vec{r}, \vec{p}, t)$ is the transport distribution function parameterized in terms of position, $\vec{r} = (x, y, z)$, momentum, $\vec{p} = (p_x, p_y, p_z)$, and time, t. In simplified terms, Eq. (2.1) can be interpreted that the time rate of the change of the distribution function, $\frac{\partial u}{\partial t}$, is equal to the sum of the change rates due to external forces, $\left(\frac{\partial u}{\partial t}\right)_{force}$, advection of the particles, $\left(\frac{\partial u}{\partial t}\right)_{advec}$, and particle-to-particle and particle-to-matter collisions, $\left(\frac{\partial u}{\partial t}\right)_{coll}$ [2].

For neutral particle transport, the following assumptions [3] about the behavior of the radiation particles can be utilized:

1. Particles may be considered as points;

2. Particles do not interact with other particles;

3. Particles interact with material target atoms in a binary manner;

4. Collisions between particles and material target atoms are instantaneous;

5. Particles do not experience any external force fields (*e.g.* gravity).

These assumptions lead to the first order form of the Boltzmann Transport Equation, which we simply call the transport equation for brevity. The remainder of the chapter is layed out as follows. Section 2.1 provides the general form of the neutron transport equation with some variants. Section 2.2 describes how we discretize the transport equation in energy with the multigroup methodology and Section 2.3 presents the angular discretization via collocation. Section 2.4 details which boundary conditions will be employed for our work. Section 2.5 will conclude our discretization procedures in the spatial domain. Section 2.6 will present the iterative procedures used to converge our solution space. We then present concluding remarks for the chapter in Section 2.7.

2.1 The Neutron Transport Equation

The time-dependent neutron angular flux, $\Psi(\vec{r}, E, \vec{\Omega}, t)$, at spatial position $\vec{r}$, with energy E moving in direction $\vec{\Omega}$ and at time t, is defined within an open, convex spatial domain $\mathcal{D}$, with boundary, $\partial\mathcal{D}$ by the general neutron transport equation:

$$\begin{aligned} \frac{\partial \Psi}{\partial t} + \vec{\Omega} \cdot \vec{\nabla} \Psi(\vec{r}, E, \vec{\Omega}, t) + \sigma_t(\vec{r}, E, t) \Psi(\vec{r}, E, \vec{\Omega}, t) &= Q_{ext}(\vec{r}, E, \vec{\Omega}, t) \\ &+ \frac{\chi(\vec{r}, E, t)}{4\pi} \int dE' \nu \sigma_f(\vec{r}, E', t) \int d\Omega' \Psi(\vec{r}, E', \vec{\Omega}', t) \\ &+ \int dE' \int d\Omega' \sigma_s(E' \rightarrow E, \Omega' \rightarrow \Omega) \Psi(\vec{r}, E', \vec{\Omega}') \end{aligned} \quad (2.2)$$

with the following, general boundary condition:

$$\Psi(\vec{r}, E, \vec{\Omega}, t) = \Psi^{inc}(\vec{r}, E, \vec{\Omega}, t) + \int dE' \int d\Omega' \gamma(\vec{r}, E' \rightarrow E, \vec{\Omega}' \rightarrow \vec{\Omega}, t)\Psi(\vec{r}, E', \vec{\Omega}', t) \quad \text{for } \vec{r} \in \partial\mathcal{D}^- \left\{\partial\mathcal{D}, \vec{\Omega}' \cdot \vec{n} < 0\right\}. \tag{2.3}$$

In Eqs. (2.2) and (2.3), the physical properties of the system are defined as the following: $\sigma_t(\vec{r}, E, t)$ is the total neutron cross section, $\chi(\vec{r}, E, t)$ is the neutron fission spectrum, $\sigma_f(\vec{r}, E', t)$ is the fission cross section, $\nu(\vec{r}, E', t)$ is the average number of neutroncs emitted per fission, $\sigma_s(E' \rightarrow E, \Omega' \rightarrow \Omega, t)$ is the scattering cross section, and $Q_{ext}(\vec{r}, E, \vec{\Omega}, t)$ is a distributed external source.

We can simplify Eq. (2.2) to:

$$\frac{\partial\Psi}{\partial t} + \mathbf{L}\Psi = \mathbf{F}\Psi + \mathbf{S}\Psi + \mathbf{Q}, \tag{2.4}$$

by dropping the dependent variable parameters and using the following operators:

$$\begin{aligned}
\mathbf{L}\Psi &= \vec{\Omega} \cdot \vec{\nabla}\Psi(\vec{r}, E, \vec{\Omega}, t) + \sigma_t(\vec{r}, E, t)\Psi(\vec{r}, E, \vec{\Omega}, t), \\
\mathbf{F}\Psi &= \frac{\chi(\vec{r}, E, t)}{4\pi} \int dE' \nu\sigma_f(\vec{r}, E', t) \int d\Omega' \Psi(\vec{r}, E', \vec{\Omega}', t), \\
\mathbf{S}\Psi &= \int dE' \int d\Omega' \sigma_s(E' \rightarrow E, \Omega' \rightarrow \Omega, t)\Psi(\vec{r}, E', \vec{\Omega}', t), \\
\mathbf{Q} &= Q_{ext}(\vec{r}, E, \vec{\Omega}, t),
\end{aligned} \tag{2.5}$$

where $\mathbf{L}$ is the loss operator which includes total reaction and streaming, $\mathbf{F}$ is the fission operator, and $\mathbf{S}$ is the scattering operator. If we wish to analyze a transport problem at steady-state conditions, we simply drop the temporal derivative to form

$$\mathbf{L}\Psi = \mathbf{F}\Psi + \mathbf{S}\Psi + \mathbf{Q}, \tag{2.6}$$

and note that the operators of Eq. (2.5) no longer depend on time, t.

There is a special subset of transport problems that is routinely analyzed to determine the neutron behavior of a fissile system called the *k-eigenvalue problem.* In Eq. (2.2), $\nu(\vec{r}, E)$ acts as a multiplicative factor on the number of neutrons emitted per fission event. We replace this multiplicative factor in the following manner:

$$\nu(\vec{r}, E) \rightarrow \frac{\tilde{\nu}(\vec{r}, E)}{k}, \tag{2.7}$$

where we have introduced the eigenvalue, k. By also dropping the external source term, the steady-state neutron transport equation in Eq. (2.6) can be rewritten into

$$(\mathbf{L} - \mathbf{S})\,\tilde{\Psi} = \frac{1}{k}\mathbf{F}\tilde{\Psi}, \tag{2.8}$$

where $(k, \tilde{\Psi})$ forms an appropriate eigenvalue-eigenvector pair. Of most interest is the eigenpair corresponding to the eigenvalue of largest magnitude.

We can then gain knowledge of the behavior of the neutron population in the problem by taking the full phase-space integrals of the loss operator $\int\int\int \mathbf{L}\tilde{\Psi}\, dE\, d\Omega\, d\vec{r}$, the fission operator $\int\int\int \mathbf{F}\tilde{\Psi}\, dE\, d\Omega\, d\vec{r}$, and the scattering operator $\int\int\int \mathbf{S}\tilde{\Psi}\, dE\, d\Omega\, d\vec{r}$. With the appropriate eigenvector solution, $\tilde{\Psi}$, the k eigenvalue then has the meaning as the multiplicative value which balances Eq. (2.8) in an integral sense. This means that k also has a physical meaning as well. A value $k < 1$ is called subcritical and corresponds to a system whose neutron population decreases in time; a value $k = 1$ is called critical and corresponds to a system whose neutron population remains constant in time; and a value $k > 1$ is called supercritical and corresponds to a system whose neutron population increases in time [4].

2.2 Energy Discretization

We begin our discretization procedures by focusing on the angular flux's energy variable. An ubiquitous energy discretization procedure in the transport community is the multigroup method [5, 6]. The multigroup method is defined by splitting the angular flux solution into G number of distinct, contiguous, and non-overlapping energy intervals called groups. We begin by restricting the full energy domain, $[0, \infty)$, into a finite domain, $E \in [E_G, E_0]$. E_0 corresponds to some maximum energy value and E_G corresponds to some minimum energy value (typically 0). We have done this by defining $G+1$ discrete energy values that are in a monotonically continuous reverse order: $E_G < E_{G-1} < \ldots < E_1 < E_0$.

From this distribution of energy values, we then say that a particular energy group, g, corresponds to the following energy interval:

$$\Delta E_g \in [E_g, E_{g-1}]. \tag{2.9}$$

Figure 2.1 provides a visual representation between the $G+1$ discrete energy values and the G energy groups. While the order that we have prescribed may seem illogical (high-to-low) to those outside of the radiation physics community, it has been historically applied this way because radiation transport problems are iteratively solved from high energy to low energy. If the group structure is well chosen, then the transport solution can be more efficiently and easily obtained.

For the remainder of this energy discretization procedure, we will utilize the steady-state form of the transport equation in Eq. (2.6). The time-dependent and eigenvalue forms are analagous and would be derived identically. Taking the energy interval for group g as defined in Eq. (2.9), the energy-integrated angular flux of group g is

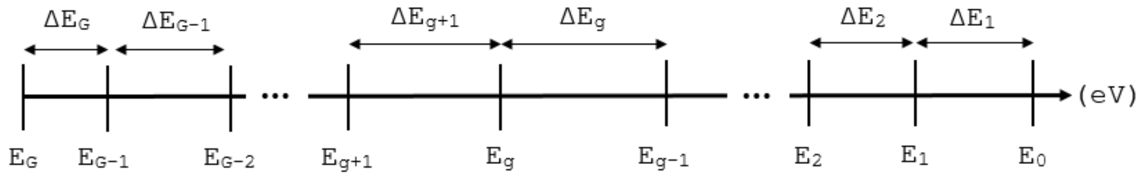

Figure 2.1: Interval structure of the multigroup methodology.

$$\Psi_g(\vec{r},\vec{\Omega}) = \int_{E_g}^{E_{g-1}} \Psi(\vec{r},E,\vec{\Omega})\,dE. \tag{2.10}$$

We can then use the energy-integrated angular flux to form the following coupled, ($g = 1, ..., G$), discrete equations (we have dropped the spatial parameter and some of the angular parameters for further clarity):

$$\left(\vec{\Omega}\cdot\vec{\nabla}+\sigma_{t,g}\right)\Psi_g = \sum_{g'=1}^{G}\left[\frac{\chi_g}{4\pi}\nu\sigma_{f,g'}\int_{4\pi}\Psi_{g'}(\vec{\Omega}')\,d\Omega' + \int_{4\pi}\sigma_s^{g'\to g}(\vec{\Omega}',\vec{\Omega})\Psi_{g'}(\vec{\Omega}')\,d\Omega'\right]+Q_g \tag{2.11}$$

where

$$\begin{aligned}
\sigma_{t,g}(\vec{r},\vec{\Omega}) &\equiv \frac{\int_{E_g}^{E_{g-1}}\sigma_t(\vec{r},\vec{\Omega},E)\Psi(\vec{r},\vec{\Omega},E)\,dE}{\int_{E_g}^{E_{g-1}}\int_{4\pi}\Psi(\vec{r},\vec{\Omega},E)\,dE} \\
\nu\sigma_{f,g}(\vec{r}) &\equiv \frac{\int_{E_g}^{E_{g-1}}\nu\sigma_f(\vec{r},E)\int_{4\pi}\Psi(\vec{r},\vec{\Omega},E)\,dEd\Omega}{\int_{E_g}^{E_{g-1}}\int_{4\pi}\Psi(\vec{r},\vec{\Omega},E)\,dEd\Omega} \\
\chi_g &\equiv \int_{E_g}^{E_{g-1}}\chi(\vec{r},E)\,dE \\
\sigma_s^{g'\to g}(\vec{r},\vec{\Omega}',\vec{\Omega}) &\equiv \frac{\int_{E_{g'}}^{E_{g'-1}}\left[\int_{E_g}^{E_{g-1}}\sigma_s(\vec{r},E'\to E,\vec{\Omega}',\vec{\Omega})\,dE\right]\Psi(\vec{r},\vec{\Omega}',E')\,dE'}{\int_{E_g}^{E_{g-1}}\Psi(\vec{r},\vec{\Omega},E)\,dE} \\
Q_g(\vec{r},\vec{\Omega}) &\equiv \int_{E_g}^{E_{g-1}}Q(\vec{r},\vec{\Omega},E)\,dE
\end{aligned} \tag{2.12}$$

The above equations are mathematically exact to those presented in Eqs. (2.2 - 2.6) and we have made no approximations at this time. However, this requires full knowledge of the energy distribution of the angular flux solution at all positions in our problem domain since we weight the multigroup cross sections with this solution. This is obviously impossible since the energy distibution is part of the solution space we are trying to solve for. Instead, we now define the process to make the multigroup discretization an effective approximation method.

We first define an approximate angular flux distribution for a region s:

$$\Psi(\vec{r}, \vec{\Omega}, E) = \hat{\Psi}(\vec{r}, \vec{\Omega}) f_s(E), \tag{2.13}$$

which is a factorization of the angular flux solution into a region-dependent energy function, $f_s(E)$, and a spatially/angularly dependent function, $\hat{\Psi}(\vec{r}, \vec{\Omega})$. With this approximation, we can redefine the energy-collapsed cross sections of Eq. (2.12):

$$\begin{aligned}
\sigma_{t,g}(\vec{r}, \vec{\Omega}) &\equiv \frac{\int_{E_g}^{E_{g-1}} \sigma_t(\vec{r}, \vec{\Omega}, E) f_s(E)\, dE}{\int_{E_g}^{E_{g-1}} f_s(E)\, dE}, \\
\nu\sigma_{f,g}(\vec{r}) &\equiv \frac{\int_{E_g}^{E_{g-1}} \nu\sigma_f(\vec{r}, E) f_s(E)\, dE}{\int_{E_g}^{E_{g-1}} f_s(E)\, dE}, \\
\sigma_s^{g' \to g}(\vec{r}, \vec{\Omega}', \vec{\Omega}) &\equiv \frac{\int_{E_{g'}}^{E_{g'-1}} \left[\int_{E_g}^{E_{g-1}} \sigma_s(\vec{r}, E' \to E, \vec{\Omega}', \vec{\Omega})\, dE \right] f_s(E')\, dE'}{\int_{E_g}^{E_{g-1}} f_s(E)\, dE}.
\end{aligned} \tag{2.14}$$

It is noted that we do not need to redefine the fission spectrum or the distributed external sources since they are not weighted with the angular flux solution. With this energy factorization, we would expect, in general, that the approximation error will tend to zero as the number of discrete energy groups increases (thereby making the energy bins thinner). This is especially true if the group structure is chosen with many more bins in energy regions with large variations in the energy solution. For certain problems, the region-dependent energy function is well understood (*i.e.* almost exactly known). This means, that for these problems, we can achieve reasonable solution accuracy with only a few groups where the energy bins of the multigroup discretization are well chosen. A good example of these kinds of problems are thermal-spectrum nuclear reactors which have historically achieved reasonable solutions with as few as 4-10 energy groups.

2.3 Angular Discretization

Now that we have provided the discretization of the energy variable, we next focus on the discretization of the transport problem in angle. We will do this in two stages: 1) expand the scattering source and the distributed external source in spherical harmonics and 2) collocate the angular flux at the interpolation points of the angular trial space. We will perform these discretization procedures by taking the stready-state equation presented in Eq. (2.6), dropping spatial parameterization, combining the fission and external sources into a single term, and using only 1 energy group:

$$\vec{\Omega} \cdot \vec{\nabla} \Psi(\vec{\Omega}) + \sigma_t \Psi(\vec{\Omega}) = \int_{4\pi} d\Omega' \, \sigma_s(\vec{\Omega}' \rightarrow \vec{\Omega}) \Psi(\vec{\Omega}') + Q(\vec{\Omega}). \tag{2.15}$$

We first develop an approximation for the scattering term in Eq. (2.15) by expanding the angular flux and the scattering cross section in spherical harmonics functions and Legendre polynomials, respectively. We begin by first assuming that the material is isotropic in relation to the radiation's initial direction. From this assumption, the parameterization of the scattering cross section can be written in terms of only the scattering angle, μ_0,

$$\sigma_s(\vec{\Omega}' \to \vec{\Omega}) = \frac{1}{2\pi}\sigma_s(\vec{\Omega}' \cdot \vec{\Omega}) = \frac{1}{2\pi}\sigma_s(\mu_0), \tag{2.16}$$

where $\mu_0 \equiv \vec{\Omega}' \cdot \vec{\Omega}$. With this simplification, the scattering cross section can now be expanded in an infinite series in terms of the Legendre polynomials,

$$\sigma_s(\vec{\Omega}' \to \vec{\Omega}) = \sum_{p=0}^{\infty} \frac{2p+1}{4\pi}\sigma_{s,p} P_p(\mu_0), \tag{2.17}$$

where $\sigma_{s,p}$ is the p angular moment of the scattering cross section. These angular moments of the scattering cross section have the form:

$$\sigma_{s,p} \equiv \int_{-1}^{1} d\mu_0 \, \sigma_s(\mu_0) P_p(\mu_0). \tag{2.18}$$

With the scattering cross section redefined, we can now expand the angular flux in terms of an infinite series of the spherical harmonics functions, Y,

$$\Psi(\vec{\Omega}) = \frac{1}{4\pi} \sum_{k=0}^{\infty} \sum_{n=-k}^{k} \Phi_{k,n} Y_{k,n}(\vec{\Omega}) \tag{2.19}$$

where the angular moments of the angular flux, $\Phi_{k,n}$, have the form:

$$\Phi_{k,n} \equiv \int_{4\pi} d\Omega \, \Psi(\vec{\Omega}) \, Y_{p,n}(\vec{\Omega}). \tag{2.20}$$

We note that the p and k orders of the scattering cross section and angular flux expansions, respectively, are not corresponding. We then take the scattering cross section expansion of Eq. (2.17) and the angular flux expansion of Eq. (2.19), and insert them into the original scattering term of the right-hand-side of Eq. (2.15). After significant algebra and manipulations, which we will not include here for brevity, the scattering term can be greatly simplified (the full details of this are located in Appendix **??**). Eq. (2.15) can now be written again with this alternate and simplified scattering term that is composed of the cross section and angular flux moments:

$$\vec{\Omega} \cdot \vec{\nabla}\Psi(\vec{\Omega}) + \sigma_t \Psi(\vec{\Omega}) = \sum_{p=0}^{\infty} \frac{2p+1}{4\pi} \sigma_{s,p} \sum_{n=-p}^{p} \Phi_{p,n} Y_{p,n}(\vec{\Omega}) + Q(\vec{\Omega}). \tag{2.21}$$

From the initial assumption of material isotropy (which may or not be an approximation), the scattering term of Eq. (2.21) has introduced no approximation. Unfortunately, this form requires an infinite series expansion which we cannot use with only finite computational resources. Instead, we truncate the series at some maximum expansion order, N_p, which, in general, introduces an approximate form for the scattering. However, we note that if the problem scattering can be exactly captured with moments through order N_p, then we have introduced no approximation with this truncation. With this order of truncation, we again write the angularly continuous Eq. (2.21), but also fold the source term into the spherical harmonics expansion,

$$\vec{\Omega} \cdot \vec{\nabla}\Psi(\vec{\Omega}) + \sigma_t \Psi(\vec{\Omega}) = \sum_{p=0}^{N_p} \frac{2p+1}{4\pi} \sum_{n=-p}^{p} Y_{p,n}(\vec{\Omega}) \left[\sigma_{s,p}\Phi_{p,n} + Q_{p,n}\right]. \tag{2.22}$$

At this point, one may wonder why we have alterred the scattering operator so that it is terms of moments of the scattering cross sections and the angular flux. The reason is two-fold which will also be discussed in further detail later in this chapter. First, it greatly reduces the phase space of the scattering cross sections. With proper preprocessing, the scattering cross sections can be simplified into just their Legendre moments, instead of having to store angle-to-angle quantities ($\vec{\Omega}' \to \vec{\Omega}$). For every

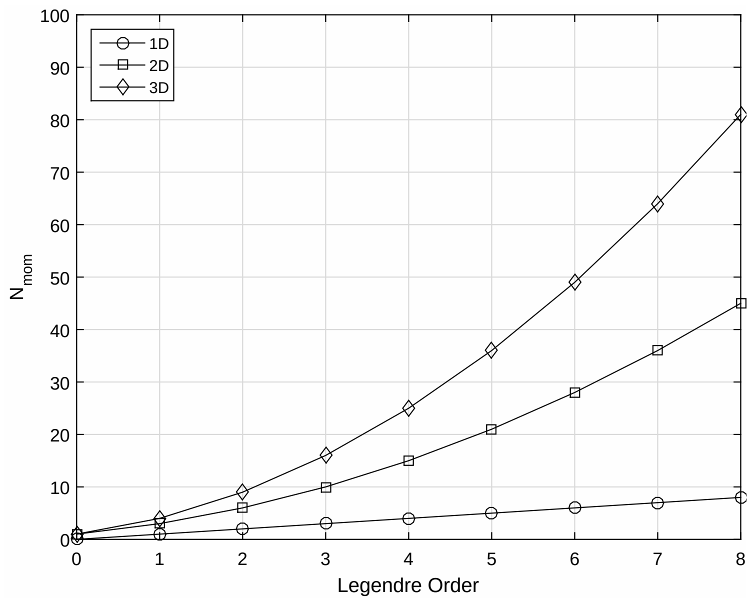

Figure 2.2: Number of spherical harmonics moments, N_{mom}, in 1D, 2D, and 3D as a function of the expansion order, p.

group-to-group combination in energy ($g' \rightarrow g$), there are only the N_p moments of the scattering cross section. Secondly, the contribution of the angular flux into the scattering source with its moments can also greatly reduce the dimensional space that needs to be stored in computer memory. This will be discussed later in further detail in Section 2.6.1, but it simply means that we only have to store N_{mom} angular flux moments for use in the scattering source. In 1 dimension, N_{mom} is equal to $(N_p + 1)$. In 2 dimensions, N_{mom} is equal to $\frac{(N_p+1)(N_p+2)}{2}$. In 3 dimensions, N_{mom} is equal to $(N_p + 1)^2$. For comparative purposes, we have plotted N_{mom} for 1,2, and 3 dimensions up to order 8 in Figure 2.2.

Up to this point, we have only presented the methodology to express our source terms with expansions of the spherical harmonics functions. Next, we describe the second portion of our angular discretization by deriving the standard S_N equations using a collocation technique. We begin by choosing a set of M distinct points and weights to form a quadrature set in angular space: $\{\vec{\Omega}_m, w_m\}_{m=1}^{M}$. We will give further details about the required characteristics of this quadrature set as well as a couple of common options a little later. Using this quadrature set, we can further define the a trial space for the angular flux,

$$\Psi(\vec{\Omega}) = \sum_{m=1}^{M} B_m(\vec{\Omega})\Psi_m, \tag{2.23}$$

where the angular bases, B_m, satisfy the *Kronecker* property,

$$B_j(\vec{\Omega}_m) = \delta_{j,m}, \tag{2.24}$$

as well as the *Lagrange* property,

$$\sum_{m=1}^{M} B_m(\vec{\Omega}_m) = 1, \tag{2.25}$$

and the singular value of the angular flux along a given direction has the following notation:

$$\Psi_m = \Psi(\vec{\Omega}_m). \tag{2.26}$$

Next, we substitute Eq. (2.23) into Eq. (2.22), drop the external source for clarity, and collocate at the interpolation (quadrature) points,

$$\vec{\Omega}\cdot\vec{\nabla}\left(\sum_{m=1}^{M}B_m(\vec{\Omega}_k)\Psi_m\right)+\sigma_t\left(\sum_{m=1}^{M}B_m(\vec{\Omega}_k)\Psi_m\right)$$
$$=\sum_{p=0}^{N_p}\frac{2p+1}{4\pi}\sigma_{s,p}\sum_{n=-p}^{p}Y_{p,n}(\vec{\Omega})\left(\sum_{m=1}^{M}\Psi_m\int_{4\pi}d\Omega\,B_m(\vec{\Omega}_k)\,Y_{p,n}(\vec{\Omega})\right),\qquad k=1,...,M \tag{2.27}$$

where we inserted Eq. (2.23) into Eq. (2.20) to form a slightly modified form for the angular flux moments:

$$\Phi_{p,n}=\sum_{m=1}^{M}\Psi_m\int_{4\pi}d\Omega\,B_m(\vec{\Omega})\,Y_{p,n}(\vec{\Omega}). \tag{2.28}$$

The *Kronecker* property of Eq. (2.24), is then used at the collocation points so that Eq. (2.27) can be simplified into the following form (where we have reintroduced the distributed source term in terms of its contribution for angle m):

$$\vec{\Omega}_m\cdot\vec{\nabla}\Psi_m+\sigma_t\Psi_m=\sum_{p=0}^{N_P}\frac{2p+1}{4\pi}\sigma_{s,p}\sum_{n=-p}^{p}Y_{p,n}(\vec{\Omega}_m)\Phi_{p,n}+Q_m\,.\qquad m=1,...,M \tag{2.29}$$

Equation (2.29) represents the transport equation that has been discretized into M separate equations in angle (for 1 energy group and no spatial discretization). Up to this point, we have simply stated that there is some angular quadrature set of size M that will satisfy some conditions of the solution, but we have not explicitly stated these conditions. For this work we will require our angular quadrature set to maintain the following properties:

1. The weights sum to 4π: $\sum_m w_m = 4\pi$.

2. The odd angular moments sum to $\vec{0}$: $\sum_m w_m \left(\vec{\Omega}_m\right)^n = \vec{0}$ $(n = 1, 3, 5, ...)$.

3. $\sum_m w_m \vec{\Omega}_m \vec{\Omega}_m = \frac{4\pi}{3}\mathbb{I}$, where $\mathbb{I}$ is the identity tensor.

4. The points and weights are symmetric about the primary axes in angular space.

5. The points and weights also need to have symmetry about the problem domain boundary (this is not an issue if the domain is a rectangle in 2D or an orthogonal parallelepiped in 3D). This point is described in greater detail in Section 2.4.

Point 4 requires some additional explanation. In 1 dimension, this corresponds to symmetry about the point 0 on the interval $[-1, 1]$. In 2 dimensions, this corresponds to quadrant-to-quadrant symmetry about the x-y primary axes of the unit circle. In 3 dimensions, this corresponds to octant-to-octant symmetry about the x-y-z primary axes of the unit sphere.

From these properties, especially property 4, our 2D and 3D quadrature sets can be constructed in a simple and consistent manner (1D quadrature sets have different construction and our work does not include them). For both 2D and 3D problems, we can generate a subset of the quadrature points and weights on a single octant of the unit sphere, where each quadrature point in this subset has the form: $\vec{\Omega}_1 = [\mu_1, \eta_1, \xi_1]$ (the '1' subscript corresponds to the primary octant). If we are solving a 2D problem, we would then project the quadrature points onto the unit circle so that they have the form: $\vec{\Omega}_1 = [\mu_1, \eta_1]$ (we can then view the primary octant as the primary quadrant). Once we have defined the quadrature points and weights for the primary quadrant or octant, we can then directly calculate the remainder of the quadrature set by mapping to the other quadrants or octants. Table 2.1 presents the mapping from the primary quadrant to the other 3 quadrants for 2D problems. Table 2.2 presents the mapping from the primary octant to the other 7 octants for

3D problems.

Table 2.1: 2D angle mapping from the first quadrant into the other 3 quadrants.

Quadrant	μ	η
1	$\mu_1 = \mu_1$	$\eta_1 = \eta_1$
2	$\mu_2 = -\mu_1$	$\eta_2 = \eta_1$
3	$\mu_3 = -\mu_1$	$\eta_3 = -\eta_1$
4	$\mu_4 = \mu_1$	$\eta_4 = -\eta_1$

Table 2.2: 3D angle mapping from the first octant into the other 7 octants.

Octant	μ	η	ξ
1	$\mu_1 = \mu_1$	$\eta_1 = \eta_1$	$\xi_1 = \xi_1$
2	$\mu_2 = -\mu_1$	$\eta_2 = \eta_1$	$\xi_2 = \xi_1$
3	$\mu_3 = -\mu_1$	$\eta_3 = -\eta_1$	$\xi_3 = \xi_1$
4	$\mu_4 = \mu_1$	$\eta_4 = -\eta_1$	$\xi_4 = \xi_1$
5	$\mu_5 = \mu_1$	$\eta_5 = \eta_1$	$\xi_5 = -\xi_1$
6	$\mu_6 = -\mu_1$	$\eta_6 = \eta_1$	$\xi_6 = -\xi_1$
7	$\mu_7 = -\mu_1$	$\eta_7 = -\eta_1$	$\xi_7 = -\xi_1$
8	$\mu_8 = \mu_1$	$\eta_8 = -\eta_1$	$\xi_8 = -\xi_1$

We conclude our discussion of angular discretizations by presenting two common angular quadrature sets that will be employed in this dissertation work. Section 2.3.1 presents the Level Symmetric (LS) quadrature set and Section 2.3.2 presents the Product Gauss-Legendre-Chebyshev (PGLC) quadrature set. Both of these quadrature sets can be formed from the procedure outlined before: form the primary octant and then map as appropriate.

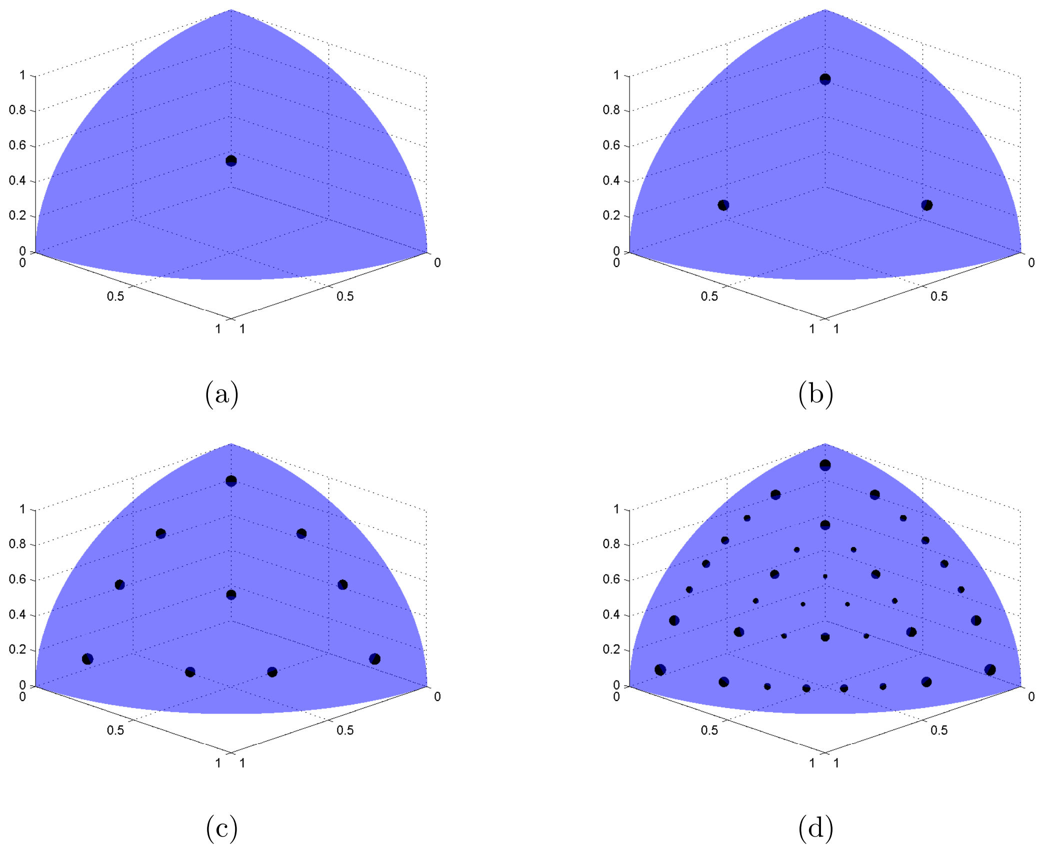

Figure 2.3: Level-Symmetric angular quadrature set of order (a) 2, (b) 4, (c) 8, and (d) 16.

2.3.1 Level Symmetric Quadrature Set

The first quadrature set we present is the common Level Symmetric set [6].

2.3.2 Product Gauss-Legendre-Chebyshev Quadrature Set

The second angular quadrature set we will present is a Product Gauss-Legendre-Chebyshev (PGLC) set. It is formed by the product-wise multiplication of a Gauss-Chebyshev quadrature in the azimuthal direction and a Gauss-Legendre quadrature in the polar direction. It has the following key differences from the Level Symmetric set:

- Does not have 90^o rotational invariance within the primary octant; still maintains octant-to-octant symmetry however;
- Has more control over the placement of the anglular directions within the primary octant;
- Quadrature weights are aligned with the polar level;
- Has strictly positive weights for all polar and azimuthal combinations.

From the listed differences, we can already discern some clear advantages and disadvantages from a fully-symmetric quadrature set like LS. If a high number of angles are required for a problem, then negative weights do not arise. This is beneficial for transport problems with significant discontinuities. Also, the quadrature directions can be preferentially distributed in the primary octant if required for a particular problem. For example, if the transport solution is smoothly varying in the polar direction and not in the azimuthal direction, then we can specify a larger number of quadrature points in the azimuthal direction, with much fewer points in the polar direction. However, this also highlights the fact that the quadrature weights are aligned with the polar level, which can lead to less accurate moment integrations for certain transport problems.

For this dissertation, we will use the following notation to define the product nature of the PGLC quadrature points: S_a^p. Here, a and p correspond to the number of azimuthal and polar directions in the primary octant, respectively. We demonstrate this definition in Figure 2.4 with several combinations of azimuthal and polar directions. Again, the size of the direction marker corresponds to the relative weight of quadrature point. One can clearly see that the weights vary on the polar levels and all azimuthal weights on a given polar level are constant.

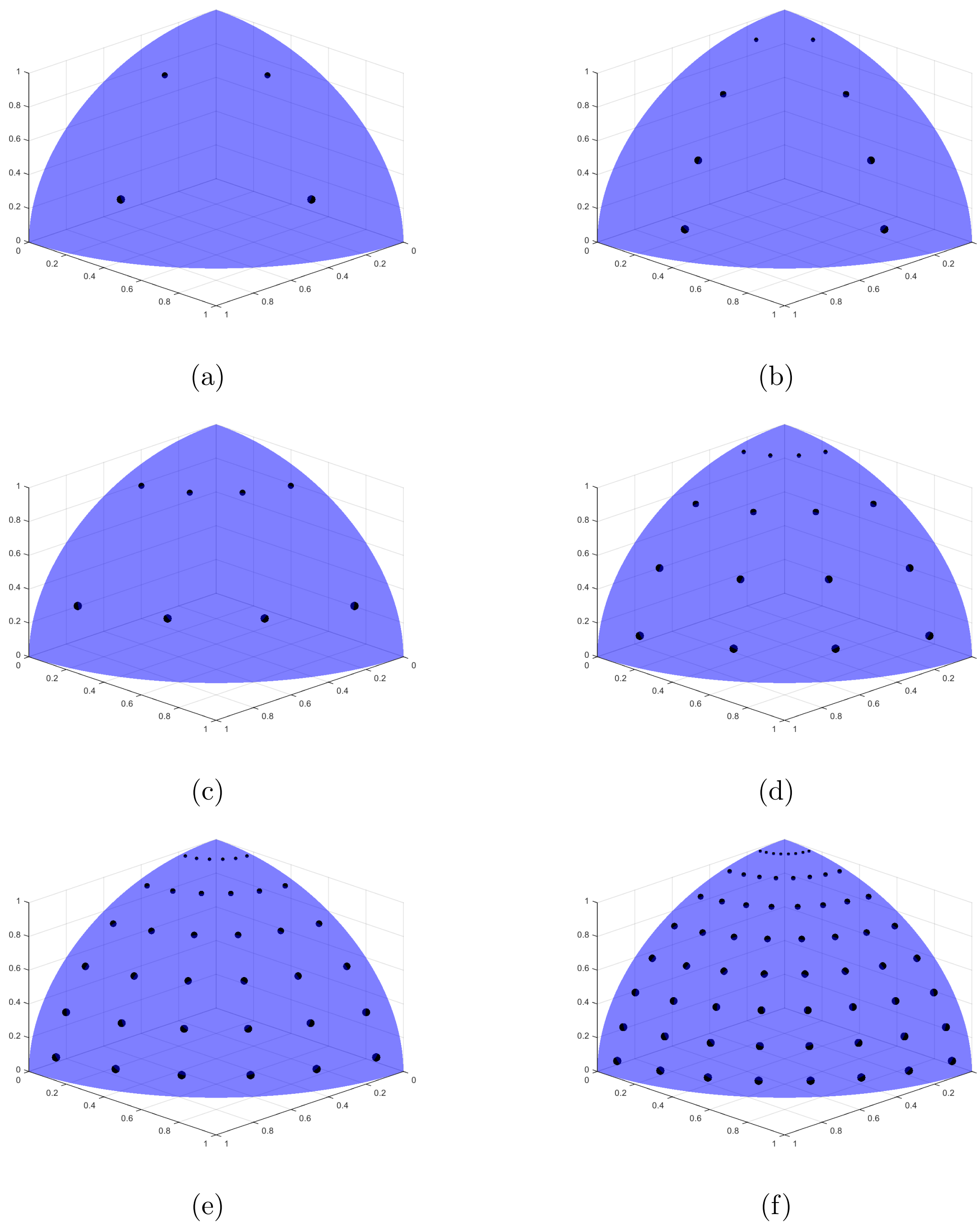

Figure 2.4: Product Gauss-Legendre-Chebyshev angular quadrature set with orders: (a) S_2^2, (b) S_2^4, (c) S_4^2, (d) S_4^4, (e) S_6^6, and (f) S_8^8.

2.4 Boundary Conditions

Using the energy and angular discretizations presented in Sections 2.2 and 2.3, respectively, we write the standard, steady-state, multigroup S_N transport equation for one angular direction, m, and one energy group, g:

$$\begin{aligned}\left(\vec{\Omega}_m \cdot \vec{\nabla} + \sigma_{t,g}\right) \Psi_{m,g} = \sum_{g'=1}^{G} \sum_{p=0}^{N_P} \frac{2p+1}{4\pi} \sigma_{s,p}^{g' \to g} \sum_{n=-p}^{p} \Phi_{p,n,g'} Y_{p,n}(\vec{\Omega}_m) \\ + \frac{\chi_g}{4\pi} \sum_{g'=1}^{G} \nu \sigma_{f,g'} \Phi_{g'} + Q_{m,g}\end{aligned}, \tag{2.30}$$

where we have dropped the spatial parameter for clarity and is beholden to the following general, discretized boundary condition:

$$\Psi_{m,g}(\vec{r}) = \Psi_{m,g}^{inc}(\vec{r}) + \sum_{g'=1}^{G} \sum_{\vec{\Omega}_{m'} \cdot \vec{n} > 0} \gamma_{g' \to g}^{m' \to m}(\vec{r}) \Psi_{m',g'}(\vec{r}). \tag{2.31}$$

These (MxG) number of discrete, tightly-coupled equations are currently defined as continuous in space.

For this dissertation work, we will consider only one type of boundary conditions: Dirichlet-type boundaries (also called *first-type boundary condition* in some physics and mathematical communities). In particular we will only utilize incoming-incident and reflecting boundary conditions which correspond to $\vec{r} \in \partial\mathcal{D}^d$ and $\vec{r} \in \partial\mathcal{D}^r$, respectively. The full domain boundary is then the union: $\partial\mathcal{D} = \partial\mathcal{D}^d \cup \partial\mathcal{D}^r$. This leads to the boundary condition being succinctly written for one angular direction, m, and one energy group, g as

$$\Psi_{m,g}(\vec{r}) = \begin{cases} \Psi_{m,g}^{inc}(\vec{r}), & \vec{r} \in \partial\mathcal{D}^d \\ \Psi_{m',g}(\vec{r}), & \vec{r} \in \partial\mathcal{D}^r \end{cases} \tag{2.32}$$

where the reflecting angle is $\vec{\Omega}_{m'} = \vec{\Omega}_m - 2\left(\vec{\Omega}_m \cdot \vec{n}\right)\vec{n}$ and $\vec{n}$ is oriented outward from the domain. To properly utilize the reflecting boundary condition that we have proposed, the angular quadrature set defined in Section 2.3 needs the following properties.

1. The reflected directions, $\vec{\Omega}_{m'}$, are also in the quadrature set for all $\vec{r} \in \partial\mathcal{D}^r$.

2. The weights of the incident, w_m, and reflected, $w_{m'}$, angles must be equal.

For problems where the reflecting boundaries align with the x, y, z axes, this will not be an issue with standard quadrature sets (*e.g.* level-symmetric or Gauss-Legendre-Chebyshev). However, if the reflecting boundaries do not align in this manner, then additional care must be employed in calculating appropriate angular quadrature sets.

2.5 Spatial Discretization

For the spatial discretization of the problem domain, we simplify Eq. (2.30) into a single energy group and drop the fission term (it can be lumped into the 0th order external source term and will act similarly to the total interaction term)

$$\vec{\Omega}_m \cdot \vec{\nabla}\Psi_m + \sigma_t\Psi_m = \sum_{p=0}^{N_P} \frac{2p+1}{4\pi} \sum_{n=-p}^{p} Y_{p,n}(\vec{\Omega}_m)\left[\sigma_{s,p}\Phi_{p,n,} + Q_{p,n}\right] \tag{2.33}$$

to form M $(m = 1, ..., M)$ angularly discrete equations. We then lay down an unstructured mesh, $\mathbb{T}_h \in \mathbb{R}^d$, over the spatial domain, where d is the dimensionality of the problem $(d = 1, 2, 3)$. This mesh consists of non-overlapping spatial elements

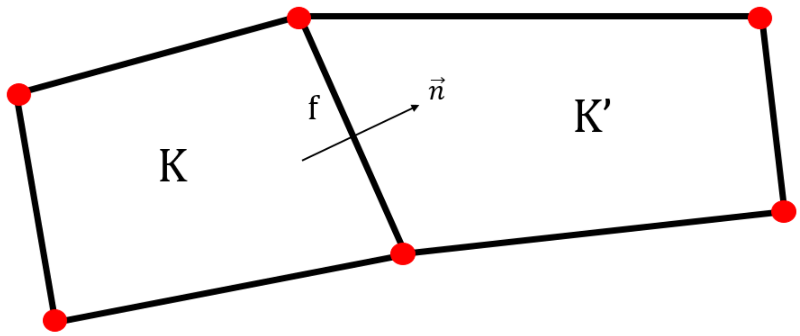

Figure 2.5: Two cells of the spatial discretization with the connecting face, f, with normal direction, $\vec{n}$, oriented from cell K to cell K'.

to form a complete union over the entire spatial domain: $\mathcal{D} = \bigcup_{K \in \mathbb{T}_h} K$. To form the DGFEM set of equations [7, 8], we consider a spatial cell $K \in \mathbb{R}^d$ which has N_V^K vertices and N_f^K faces. Each face of cell K resides in dimension $\mathbb{R}^{d-1}$ and is formed by a connection of a subset of vertices. For a 1D problem, each face is a single point. For a 2D problem, each face is a line segment connecting two distinct points. For a 3D problem, each face is a $\mathbb{R}^2$ closed polygon (not necessarily coplanar) which may or not be convex. An example of this interconnection between elements is given for a $\mathbb{R}^2$ problem in Figure 2.5 between our cell of interest, K, and another cell, K', separated by the face f. We have chosen the normal direction of the face to have orientation from cell K to cell K' while we form the DGFEM equations for cell K. This means that if we were instead analyzing cell K', then the face f normal, $\vec{n}'$, would be opposite (*i.e.* $\vec{n}' = -\vec{n}$).

Next, we left-multiply Eq. (2.33) by an appropriate test function b_m, integrate over cell K, and apply Gauss' Divergence Theorem to the streaming term to obtain the Galerkin weighted-residual for cell K for an angular direction $\vec{\Omega}_m$:

$$
\begin{aligned}
&-\left(\vec{\Omega}_m \cdot \vec{\nabla} b_m, \Psi_m\right)_K + \sum_{f=1}^{N_f^K} \left\langle (\vec{\Omega}_m \cdot \vec{n})\, b_m, \tilde{\Psi}_m \right\rangle_f + \left(\sigma_t b_m, \Psi_m\right)_K \\
&= \sum_{p=0}^{N_P} \sum_{n=-p}^{p} \frac{2p+1}{4\pi} Y_{p,n}(\vec{\Omega}_m) \left[\left(\sigma_{s,p}\, b_m, \Phi_{p,n,}\right)_K + \left(b_m, Q_{p,n}\right)_K \right]
\end{aligned}
. \tag{2.34}
$$

The cell boundary fluxes, $\tilde{\Psi}_m$, will depend on the cell boundary type and will be defined shortly. The cell boundary $\partial\mathcal{D}_K = \bigcup_{f \in N_f^K} f$ is the closed set of the N_f^K faces of the geometric cell. The inner products:

$$
\left(f, g\right)_K \equiv \int_K f\, g\, dr \tag{2.35}
$$

and

$$
\left\langle f, g \right\rangle_f \equiv \int_f f\, g\, ds \tag{2.36}
$$

correspond to integrations over the cell and faces, respectively, where $dr \in \mathbb{R}^d$ is within the cell and $ds \in \mathbb{R}^{d-1}$ is along the cell boundary. We note that we will use this notation of the inner product for the remainder of the dissertation unless otherwise stated. We then separate the summation of the cell K boundary integration terms into two different types: outflow boundaries ($\partial K^+ = \{\vec{r} \in \partial K : \vec{n}(\vec{r}) \cdot \vec{\Omega}_m > 0\}$) and inflow boundaries ($\partial K^- = \{\vec{r} \in \partial K : \vec{n}(\vec{r}) \cdot \vec{\Omega}_m < 0\}$). The inflow boundaries can further be separated into inflow from another cell: $\partial K^- \backslash \partial\mathcal{D}$; inflow from incident flux on the domain boundary: $\partial K^- \cap \partial\mathcal{D}^d$; and reflecting domain boundaries: $\partial K^- \cap \partial\mathcal{D}^r$. At this point, we note that the derivation can comprise an additional step by using Gauss' Divergence Theorem again on the streaming term. This is sometimes performed for radiation transport work so that mass matrix lumping can be performed, but we will not do so here. Therefore, with the cell boundary terminology as proposed, Eq. (2.34) can be written into the following form:

$$\begin{aligned} & -\Big(\vec{\Omega}_m \cdot \vec{\nabla} b_m, \Psi_m\Big)_K + \Big(\sigma_t b_m, \Psi_m\Big)_K \\ & + \Big\langle (\vec{\Omega}_m \cdot \vec{n})\, b_m, \tilde{\Psi}_m \Big\rangle_{\partial K^+} + \Big\langle (\vec{\Omega}_m \cdot \vec{n})\, b_m, \tilde{\Psi}_m \Big\rangle_{\partial K^- \backslash \partial \mathcal{D}} \\ & + \Big\langle (\vec{\Omega}_m \cdot \vec{n})\, b_m, \tilde{\Psi}_m \Big\rangle_{\partial K^- \cap \partial \mathcal{D}^d} + \Big\langle (\vec{\Omega}_m \cdot \vec{n})\, b_m, \tilde{\Psi}_m \Big\rangle_{\partial K^- \cap \partial \mathcal{D}^r} . \\ & = \sum_{p=0}^{N_P} \sum_{n=-p}^{p} \frac{2p+1}{4\pi} Y_{p,n}(\vec{\Omega}_m) \left[\Big(\sigma_{s,p}\, b_m, \Phi_{p,n,}\Big)_K + \big(b_m, Q_{p,n}\big)_K \right] \end{aligned} \tag{2.37}$$

We can now deal with the boundary fluxes, $\tilde{\Psi}_m$, by enforcing the ubiquitously-used *upwind scheme*. In simple nomenclature, the upwind scheme corresponds to using the angular flux values within the cell for outflow boundaries and angular flux values outside the cell for inflow boundaries. Mathematically, the upwind scheme can succinctly be written as the following for all boundary types,

$$\tilde{\Psi}_m(\vec{r}) = \begin{cases} \Psi_m^-, & \partial K^+ \\ \Psi_m^+, & \partial K^- \backslash \partial \mathcal{D} \\ \Psi_m^{inc}, & \partial K^- \cap \partial \mathcal{D}^d \\ \Psi_{m'}^-, & \partial K^- \cap \partial \mathcal{D}^r \end{cases}, \tag{2.38}$$

when the following trace is applied to the angular fluxes :

$$\Psi_m^{\pm}(\vec{r}) \equiv \lim_{s \to 0^{\pm}} \Psi_m\Big(\vec{r} + s(\vec{\Omega}_m \cdot \vec{n})\vec{n}\Big). \tag{2.39}$$

This trace has the notation, with $\vec{n}$ pointing outwards from cell K, of Ψ_m^- corresponding to fluxes within the cell and Ψ_m^+ corresponding to fluxes out of the cell. Now, using the upwind scheme as previously defined, we can write our complete set of DGFEM equations for cell K as

$$
\begin{aligned}
&-\left(\vec{\Omega}_m\cdot\vec{\nabla} b_m, \Psi_m\right)_K + \left(\sigma_t b_m, \Psi_m\right)_K + \left\langle (\vec{\Omega}_m \cdot \vec{n})\, b_m, \Psi_m^-\right\rangle_{\partial K^+} \\
&\quad + \left\langle (\vec{\Omega}_m \cdot \vec{n})\, b_m, \Psi_m^+\right\rangle_{\partial K^- \setminus \partial \mathcal{D}} + \left\langle (\vec{\Omega}_m \cdot \vec{n})\, b_m, \Psi_{m'}^-\right\rangle_{\partial K^- \cap \partial \mathcal{D}^r} \\
&\quad = \sum_{p=0}^{N_P} \sum_{n=-p}^{p} \frac{2p+1}{4\pi} Y_{p,n}(\vec{\Omega}_m) \left[\left(\sigma_{s,p}\, b_m, \Phi_{p,n,}\right)_K + \left(b_m, Q_{p,n}\right)_K \right] \\
&\quad + \left\langle (\vec{\Omega}_m \cdot \vec{n})\, b_m, \Psi_m^{inc}\right\rangle_{\partial K^- \cap \partial \mathcal{D}^d}
\end{aligned}
\qquad (2.40)
$$

We note that fluxes without the trace superscript are all within the cell. By completely defining our mathematical formulation for an arbitrary spatial cell, it is easy to see that the full set of equations to define our discretized solution space for a single angle and energy group comprises of a simple double integration loop. The full set of equations can be formed by looping over all spatial cells, $\mathcal{D} = \bigcup_{K \in \mathbb{T}_h} K$, while further looping over all faces within each cell, $\partial \mathcal{D}_K = \bigcup_{f \in N_f^K} f$. Section 2.6 will further detail how all the DGFEM equations are formed along with efficient solution methods. We conclude this section by defining the elementary matrix terms for a given cell as follows.

2.5.1 Elementary Mass Matrices

In the spatially discretized equations presented in Section 2.5, there are several reaction terms that appear with the form: $\left(\sigma b_m, \Psi_m\right)_K$ for a given angular direction, m, and for a spatial cell, K. In FEM analysis these reaction terms are ubiquitously referred to as the mass matrix terms [9, 10]. For cell K, we define the elementary mass matrix, $\mathbf{M}$ as

$$
\mathbf{M}_K = \int_K \mathbf{b}_K\, \mathbf{b}_K^T\, dr, \qquad (2.41)
$$

where $\mathbf{b}_K$ corresponds to the set of N_K basis functions that have non-zero measure in cell K. Depending on the FEM basis functions utilized, the integrals in Eq. (2.41) can be directly integrated analytically. However, if in general, the basis functions cannot be analytically integrated on an arbitrary set of cell shapes, then a numerical integration scheme becomes necessary. If we define a quadrature set, $\left\{\vec{x}_q, w_q^K\right\}_{q=1}^{N_q}$, for cell K, consisting of N_q points, $\vec{x}_q$, and weights, w_q^K, then we can numerically calculate the mass matrix by the following

$$\mathbf{M}_K = \sum_{q=1}^{N_q} w_q^K \mathbf{b}_K(\vec{x}_q)\, \mathbf{b}_K^T(\vec{x}_q). \tag{2.42}$$

In this case, it is necessary that the sum of the weights of this quadrature set exactly equal the geometric measure of cell K. This means that $\sum_{q=1}^{N_q} w_q^K$ is equal to the cell width in 1 dimension, the cell area in 2 dimensions, and the cell volume in 3 dimensions.

Since $\mathbf{b}_K$ consists of a column vector for the basis functions and $\mathbf{b}_K^T$ consists of a row vector, then their multiplication will obviously yield a full $(N_K \,\mathrm{x}\, N_K)$ matrix. This matrix is written for completeness of this discussion on the mass matrix:

$$\mathbf{M}_K = \begin{bmatrix} \int_K b_1\, b_1 & \dots & \int_K b_1\, b_j & \dots & \int_K b_1\, b_{N_K} \\ \vdots & & \vdots & & \vdots \\ \int_K b_i\, b_1 & \dots & \int_K b_i\, b_j & \dots & \int_K b_i\, b_{N_K} \\ \vdots & & \vdots & & \vdots \\ \int_K b_{N_K}\, b_1 & \dots & \int_K b_{N_K}\, b_j & \dots & \int_K b_{N_K}\, b_{N_K} \end{bmatrix}, \tag{2.43}$$

where an individual matrix entry is of the form:

$$M_{i,j,K} = \int_K b_i\, b_j. \tag{2.44}$$

2.5.2 Elementary Streaming Matrices

Next, we will consider the streaming term that has the form: $\left(\vec{\Omega}_m \cdot \vec{\nabla} b_m, \Psi_m\right)_K$ for a given angular direction, m, and for a spatial cell, K. $\vec{\nabla}$ is the gradient operator in physical space. It has the form of $\vec{\nabla} = \left[\frac{d}{dx}\right]$ in 1 dimension, the form of $\vec{\nabla} = \left[\frac{\partial}{\partial x}, \frac{\partial}{\partial y}\right]$ in 2 dimensions, and the form of $\vec{\nabla} = \left[\frac{\partial}{\partial x}, \frac{\partial}{\partial y}, \frac{\partial}{\partial z}\right]$ in 3 dimensions. Since for every cell, the streaming term is applied for all M angles in the angular discretization, we define the analytical elementary streaming matrix:

$$\vec{\mathbf{G}}_K = \int_K \vec{\nabla} \mathbf{b}_K \, \mathbf{b}_K^T \, dr, \tag{2.45}$$

which has dimensionality (N_KxN_Kxd). We choose to store the elementary streaming matrix in this form and not store M separate (N_KxN_K) local matrices corresponding to the application of the dot product ($\vec{\Omega}_m \cdot \int_K \vec{\nabla} \mathbf{b}_K \, \mathbf{b}_K^T \, dr$). Instead we simply evaluate the dot product with the appropriate angular direction whenever necessary. This has great benefit when trying to run large transport problems when memory becomes a premium and processor operations are not our limiting bottleneck.

Just like the elementary mass matrix, we can use the same spatial quadrature set, $\left\{\vec{x}_q, w_q^K\right\}_{q=1}^{N_q}$, for cell K to numerically calculate the streaming matrix:

$$\vec{\mathbf{G}}_K = \sum_{q=1}^{N_q} w_q^K \vec{\nabla} \mathbf{b}_K(\vec{x}_q) \, \mathbf{b}_K^T(\vec{x}_q). \tag{2.46}$$

In this case, this local cell-wise streaming matrix has the full matrix form:

$$
\vec{\mathbf{G}}_K = \begin{bmatrix} \int_K \vec{\nabla} b_1 \, b_1 & \dots & \int_K \vec{\nabla} b_1 \, b_j & \dots & \int_K \vec{\nabla} b_1 \, b_{N_K} \\ \vdots & & \vdots & & \vdots \\ \int_K \vec{\nabla} b_i \, b_1 & \dots & \int_K \vec{\nabla} b_i \, b_j & \dots & \int_K \vec{\nabla} b_i \, b_{N_K} \\ \vdots & & \vdots & & \vdots \\ \int_K \vec{\nabla} b_{N_K} \, b_1 & \dots & \int_K \vec{\nabla} b_{N_K} \, b_j & \dots & \int_K \vec{\nabla} b_{N_K} \, b_{N_K} \end{bmatrix}, \tag{2.47}
$$

where an individual matrix entry is of the form:

$$
\vec{G}_{i,j,K} = \int_K \vec{\nabla} b_i \, b_j . \tag{2.48}
$$

2.5.3 Elementary Surface Matrices

Finally, the last terms to consider of the discretized transport equation are those found on the faces of the cell boundary: $\vec{\Omega}_m \cdot \left\langle \vec{n} \, b_m, \Psi_m \right\rangle_{\partial K}$. These terms are analagous to the cell mass matrix but are computed on the cell boundary with dimensionality $(d-1)$. Analyzing a single face, f, in cell K, the analytical surface matrix is of the form,

$$
\vec{\mathbf{F}}_{f,K} = \int_f \vec{n}(\vec{r}) \, \mathbf{b}_K \, \mathbf{b}_K^T \, ds, \tag{2.49}
$$

where we allow the outward surface normal, $\vec{n}$, to vary along the cell face. For 1D problems as well as 2D problems with colinear cell faces (no curvature), the outward normals would be constant along the entire face. However, there are many cases where 3D mesh cells would not have coplanar vertices along a face. Then, the outward normal would not be constant along the face and would need to be taken into account during integration procedures. A simple example of non-coplanar face vertices would be an orthogonal hexahedral cell that has its vertices undergo a randomized displacement.

With the analytical form of the surface matrices defined in Eq. (2.49), we can see that they have dimensionality, (N_KxN_Kxd). This is the same dimensionality as the cell streaming term. However, it is possible to reduce the dimensionality of the surface matrices if it is desired to reduce the memory footprint. There are some basis sets where all but $N_b^{f,K}$ basis functions are zero along face f. If we also restrict the mesh cell faces of our transport problems to have colinear (in 2D) or coplanar (in 3D) vertices so that the outward normal is constant along a face f, then we can define the surface matrix as $\int_f \mathbf{b}_K \, \mathbf{b}_K^T \, ds$. For these basis sets with $N_b^{f,K}$ non-zero face values on colinear/coplanar face f, the surface matrix has reduced dimensionality of ($N_b^{f,K}$x$N_b^{f,K}$).

Just like the cell mass and streaming matrices, it is possible that the basis functions cannot be integrated analytically. Analogous to the cell-wise quadrature, we can define a quadrature set for face face f: $\left\{ \vec{x}_q, w_q^f \right\}_{q=1}^{N_q^f}$. This quadrature set is not specific for just one of the cells that face f separates. If the quadrature set can exactly integrate the basis functions of both cells K and K' (as defined by Figure 2.5), then only 1 quadrature set needs to be defined for both cells. Using this quadrature set, we can numerically calculate the surface matrix for face f along cell K:

$$\vec{\mathbf{F}}_{f,K} = \sum_{q=1}^{N_q^f} w_q^f \vec{n}(\vec{x}_q) \, \mathbf{b}_K(\vec{x}_q) \, \mathbf{b}_K^T(\vec{x}_q). \tag{2.50}$$

Similar to the cell-wise spatial quadrature sets, the sum of the weights of these face-wise quadrature sets need to exactly equal the geometric measure of face f. This means that $\sum_{q=1}^{N_q^f}$ is equal to 1.0 in 1 dimension, the length of the face edge in 2 dimensions and the face area in 3 dimensions.

Using the same notation as the cell-wise mass and streaming matrices, the local face-wise surface matrix for face f has the full matrix form,

$$\vec{\mathbf{F}}^{f,K} = \begin{bmatrix} \int_f \vec{n}\, b_1\, b_1 & \dots & \int_f \vec{n}\, b_1\, b_j & \dots & \int_f \vec{n}\, b_1\, b_{N_K} \\ \vdots & & \vdots & & \vdots \\ \int_f \vec{n}\, b_i\, b_1 & \dots & \int_f \vec{n}\, b_i\, b_j & \dots & \int_f \vec{n}\, b_i\, b_{N_K} \\ \vdots & & \vdots & & \vdots \\ \int_f \vec{n}\, b_{N_K}\, b_1 & \dots & \int_f \vec{n}\, b_{N_K}\, b_j & \dots & \int_f \vec{n}\, b_{N_K}\, b_{N_K} \end{bmatrix}, \tag{2.51}$$

where an individual matrix entry is of the form:

$$\vec{F}_{i,j,f,K} = \int_f \vec{n}\, b_i\, b_j. \tag{2.52}$$

2.6 Solution Procedures

To this point, we have properly described the procedures to discretize the transport problem in energy, angle, and space. We now spend the remainder of this chapter discussing various methodologies to efficiently solve the tightly-coupled system of equations composing our transport problem. Section 2.6.1 details the iterative procedures used to solve the transport problem in energy and angle, and Section 2.6.2 then describes how we solve the spatial portion of the problem for a single energy/angle iteration.

2.6.1 Angle and Energy Iteration Procedures

The fully discretized transport equation has an angular flux solution, $\mathbf{\Psi}$, with dimensionality of $(G\text{x}M\text{x}N_{dof})$. The angular flux moments, $\mathbf{\Phi}$, have dimensionality of $(G\text{x}N_{mom}\text{x}N_{dof})$. Depending on the necessary fidelity of the problem, the full phase-space of the solution can become extremely large to solve. We can have *billions* of total unkowns to solve for if we simply have $N_{dof} \approx O(10^6)$, $M \approx O(10^2)$, and

$G \approx O(10^1)$.

In theory, if we had the computer memory, we could construct a left-hand-side matrix of dimensionality $(G\text{x}M\text{x}N_{dof})\text{x}(G\text{x}M\text{x}N_{dof})$ with a corresponding right-hand-side vector of dimensionality $(G\text{x}M\text{x}N_{dof})\text{x}1$, we could then directly solve for the full phase-space angular flux solution at once. However, because the dimensional space of the unknowns can rapidly grow and become to large for hardware memory, transport problems have traditionally been solved iteratively. We now detail the procedures that we will employ to iteratively obtain the phase-space solution in energy and angle.

$$\begin{aligned} \mathbf{L}\mathbf{\Psi} - \mathbf{M}\mathbf{\Sigma}\mathbf{\Phi} &= \mathbf{Q} \\ \mathbf{\Phi} &= \mathbf{D}\mathbf{\Psi} \end{aligned} \tag{2.53}$$

where $\mathbf{L}$ is the fully-discretized loss operator which consists of total interaction and streaming terms, $\mathbf{M}$ is the moment-to-discrete operator of the angular discretization, $\mathbf{D}$ is the discrete-to-moment operator of the angular discretization, $\mathbf{\Sigma}$ is the scattering operator of the multigroup and angular discretizations, and $\mathbf{Q}$ is the full phase-space distributed source. In this case the source contains contributions from boundary and domain sources, fission sources, and scattering sources from outside the group set into the group set of interest.

$$\left(\mathbf{I} - \mathbf{T}\right)\mathbf{\Phi} = \mathbf{D}\mathbf{L}^{-1}\mathbf{Q} \tag{2.54}$$

where we define,

$$\mathbf{T} \equiv \mathbf{D}\mathbf{L}^{-1}\mathbf{M}\mathbf{\Sigma}, \tag{2.55}$$

for further brevity.

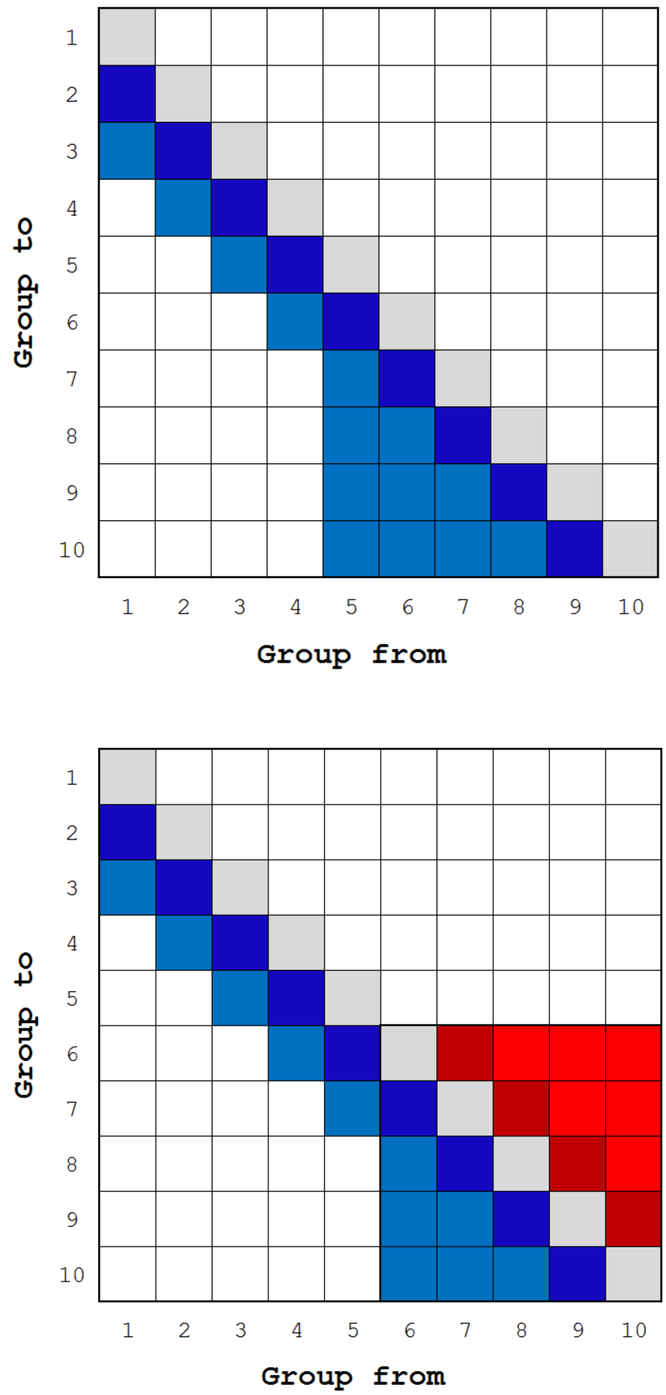

Figure 2.6: Scattering matrices (top) without and (bottom) with upscattering. The gray corresponds to within-group scattering; the blue corresponds to down-scattering in energy; and the red corresponds to up-scattering in energy.

2.6.1.1 Source Iteration

One simple method to invert $(\mathbf{I}-\mathbf{T})$ of Eq. (2.54) is the *source iteration* technique, also known as *richardson iteration*.

$$\begin{aligned} \mathbf{\Psi}^{(\ell+1)} &= \mathbf{L}^{-1}\mathbf{M}\mathbf{\Sigma}\mathbf{\Phi}^{(\ell)} + \mathbf{L}^{-1}\mathbf{Q} \\ \mathbf{\Phi}^{(\ell+1)} &= \mathbf{D}\mathbf{\Psi}^{(\ell+1)} \end{aligned} \tag{2.56}$$

2.6.1.2 Krylov Subspace Methods - GMRES

2.6.2 Spatial Solution Procedures

Section 2.6.1 presented the methodology that we will employ to iteratively converge our transport solutions in energy and angle (flux moments). Both richardson iteration and GMRES were presented as methods that can invert the $(\mathbf{I}-\mathbf{T})$ operator. In both of these iterative methods, the common operation of interest is the inversion of the loss operator ($\mathbf{L}$). There are different techniques that could be used to perform this operation, including serveral matrix-dependent and matrix-free methodologies. For this work, we will utilize the full-domain transport sweep as we outline next in Section 2.6.2.1.

2.6.2.1 Transport Sweeping

The full-domain transport sweep is a beneficial matrix-free scheme because of the following:

- The number of sweep iterations does not grow with increasing problem size or processor counts. This is in contrast with partial-domain sweeping like *parallel block jacobi* (PBJ) [11].
- Does not require the formation of M separate matrices for each of the angular

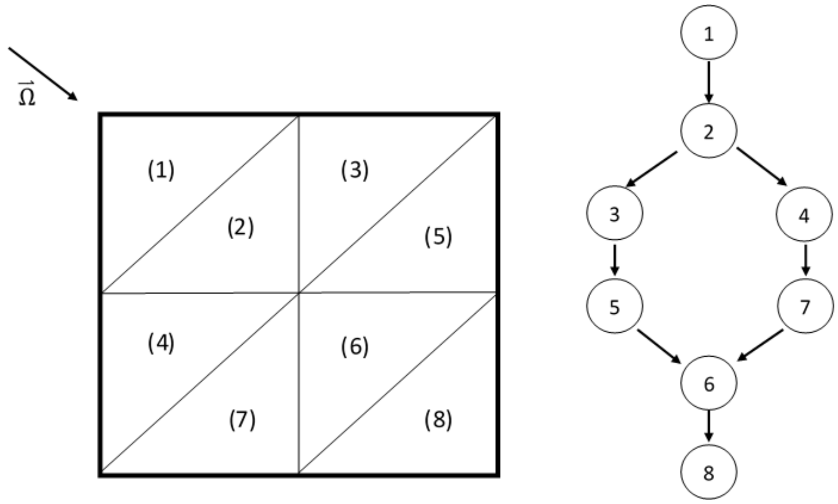

Figure 2.7: blah.

directions.

•

2.6.2.2 Spatial Adaptive Mesh Refinement

$$\eta_K^r = \int_{\partial K} [\![\Phi^r]\!]^2 d\,s = \int_{\partial K} \left(\sum_m w_m [\![\Psi_m^r]\!] \right)^2 \tag{2.57}$$

where $[\![\cdot]\!]$ is the jump operator along a face defined as,

$$[\![\Phi(\vec{r})]\!] = \Phi^+(\vec{r}) - \Phi^-(\vec{r}), \tag{2.58}$$

and the terms,$\Phi^+(\vec{r})$ and $\Phi^-(\vec{r})$, are subject to the trace:

$$\Phi^{\pm}(\vec{r}) = \lim_{s \to 0^{\pm}} \Phi(\vec{r} + s\vec{n}). \tag{2.59}$$

In this case, the outward normal, $\vec{n}$, is determined with respect to the element K along its boundary, ∂K. With this trace, $\Phi^-(\vec{r})$ always corresponds to the solution

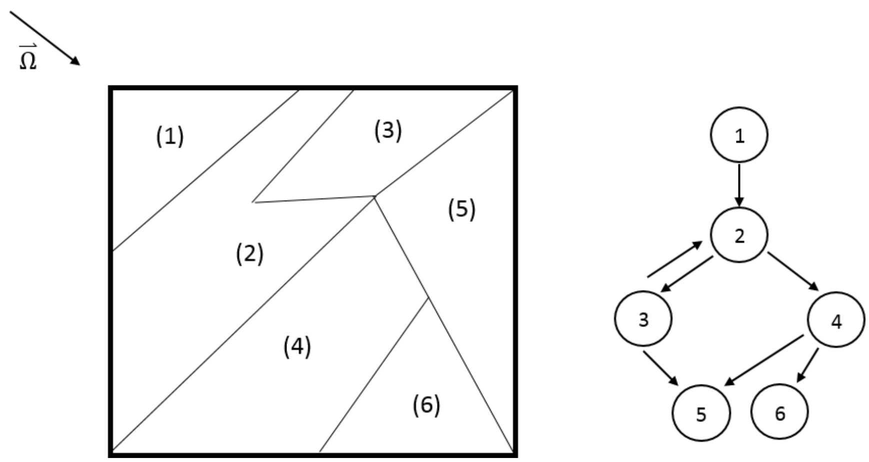

Figure 2.8: blah.

within cell K. Investigating face f of cell K, the across-face solution, $\Phi^{+}(\vec{r})$, is dependent on the boundary type of face f. The across-face solutions can be succinctly writen:

$$\Phi^{+}(\vec{r}) = \begin{cases} \lim_{s \to 0^{+}} \Phi(\vec{r} + s\vec{n}) & \vec{r} \notin \partial\mathcal{D} \\ \sum_{\vec{\Omega}_m \cdot \vec{n} > 0} \Psi_m^{-}(\vec{r}) + \sum_{\vec{\Omega}_m \cdot \vec{n} < 0} \Psi_m^{inc}(\vec{r}) & \vec{r} \in \partial\mathcal{D}^{d} \\ \Phi^{-}(\vec{r}) & \vec{r} \in \partial\mathcal{D}^{r} \end{cases} . \tag{2.60}$$

From Eq. (2.60), the across-face solutions for interior faces, incident boundaries and reflecting boundaries have different meanings. For an interior face f ($\vec{r} \notin \partial\mathcal{D}$), the across-face solution comes from the cell K' (as defined by Figure 2.5). For incident boundaries ($\vec{r} \in \partial\mathcal{D}^{d}$), the across-face solution is a combination of integrals of the outgoing (Ψ_m^{-}) and incident boundary fluxes (Ψ_m^{inc}). Finally, for reflecting boundaries ($\vec{r} \in \partial\mathcal{D}^{r}$), the across-face solutions are simply the within-cell solutions. Therefore, the solution jump is exactly zero for all reflecting boundaries and yields no contribution to the error estimate.

$$\eta_K^r \geq \alpha \max_{K' \in \mathbb{T}_h^r} \left(\eta_{K'}^r \right) \tag{2.61}$$

where α is a user-defined value $(0, 1)$. This refinement criterion has a simple meaning. If, for example, $\alpha = 0.2$, then a cell will be refined if its error estimate is greater than 20% of the cell with the largest error estimate. This does not necessarily mean that 80% of the mesh cells will be refined at level r. Instead, the criterion simply states that any cell above a particular threshold will be refined. This means that it is theoretically possible for the extreme cases of 1 or all cells being refined at a particular refinement cycle.

2.7 Conclusions

In this chapter, we have presented the tightly-coupled system of equations that comprise the DGFEM S_N transport equation. We began with the fully-continuous transport equation presented in Section 2.1 and then discretized it in energy, angle and space in Sections 2.2, 2.3, and 2.5, respectively. Appropriate boundary conditions were presented in Section 2.4. For this work, we will only utilize incoming-incident and reflecting boundary conditions and not use any further albedo terms. We finished this chapter in Section 2.6 by describing the procedures that will be utilized to solve our system of equations.

3. FEM BASIS FUNCTIONS FOR UNSTRUCTURED POLYTOPES

In Section 2.5, we detailed the spatial discretization of the transport equation. We then proceeded to give the functional forms for the various

3.1 Linear Basis Functions on 2D Polygons

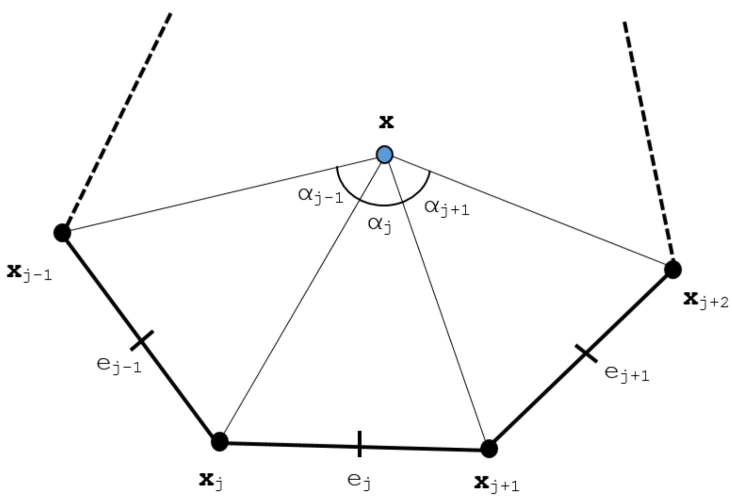

Figure 3.1: Arbitrary polygon with geometric properties used for 2D basis function generation.

In this dissertation, all 1st-order, two-dimensional basis functions for a cell will obey the properties for barycentric coordinates. They will form a *partition of unity*,

$$\sum_{i=1}^{N_K} b_i(\vec{x}) = 1; \tag{3.1}$$

coordinate interpolation will result from an *affine combination* of the vertices,

$$\sum_{i=1}^{N_K} b_i(\vec{x})\vec{x}_i = \vec{x}; \tag{3.2}$$

and they will satisfy the *Lagrange property*,

$$b_i(\vec{x}_j) = \delta_{ij}. \tag{3.3}$$

N_K is again the number of spatial degrees with measure in element K. Using the *partition of unity* of Eq. (3.1), we can rewrite Eqs. (3.1-3.2) into a separate, compact, vectorized form for completeness

$$\sum_{i=1}^{N_K} b_i(\vec{x})\vec{c}_{i,1}(\vec{x}) = \vec{q}_1, \tag{3.4}$$

where $\vec{c}_{i,1}(\vec{x})$ and $\vec{q}_1$ are the lineary-complete constraint and equivalence terms, respectively. These terms are simply:

$$\vec{c}_{i,1}(\vec{x}) = \begin{bmatrix} 1 \\ x_i - x \\ y_i - y \end{bmatrix} \qquad \text{and} \qquad \vec{q}_1 = \begin{bmatrix} 1 \\ 0 \\ 0 \end{bmatrix}, \tag{3.5}$$

respectively.

3.1.1 Traditional Linear Basis Functions - $\mathbb{P}_1$ and $\mathbb{Q}_1$ Spaces

Before presenting basis function sets applicable to polytope finite elements, we first provide two common basis functions that are exact on triangles and convex quadrilaterals: the $\mathbb{P}_1$ and $\mathbb{Q}_1$ spaces, respectively.

$$\begin{aligned} b_1(r,s) &= 1 - r - s \\ b_2(r,s) &= r \\ b_3(r,s) &= s \end{aligned} \tag{3.6}$$

and

$$
\begin{aligned}
b_1(r,s) &= (1-r)(1-s) \\
b_2(r,s) &= r(1-s) \\
b_3(r,s) &= rs \\
b_4(r,s) &= (1-r)s
\end{aligned} \tag{3.7}
$$

3.1.2 Wachspress Rational Basis Functions

$$
b_j^W(\vec{x}) = \frac{w_j(\vec{x})}{\sum_i w_i(\vec{x})} \tag{3.8}
$$

where the weight function for vertex j, w_j, has the following definition:

$$
w_j(\vec{x}) = \frac{A(\vec{x}_{j-1}, \vec{x}_j, \vec{x}_{j+1})}{A(\vec{x}, \vec{x}_{j-1}, \vec{x}_j)\, A(\vec{x}, \vec{x}_j, \vec{x}_{j+1})} \tag{3.9}
$$

3.1.3 Piecewise Linear (PWL) Basis Functions

$$
b_j^{PWL}(x,y) = t_j(x,y) + \alpha_j^K t_c(x,y) \tag{3.10}
$$

t_j is the standard 2D linear function with unity at vertex j that linearly decreases to zero to the cell center and each adjoining vertex. t_c is the 2D cell "tent" function which is unity at the cell center and linearly decreases to zero to each cell vertex. α_j^K is the weight parameter for vertex j in cell K.

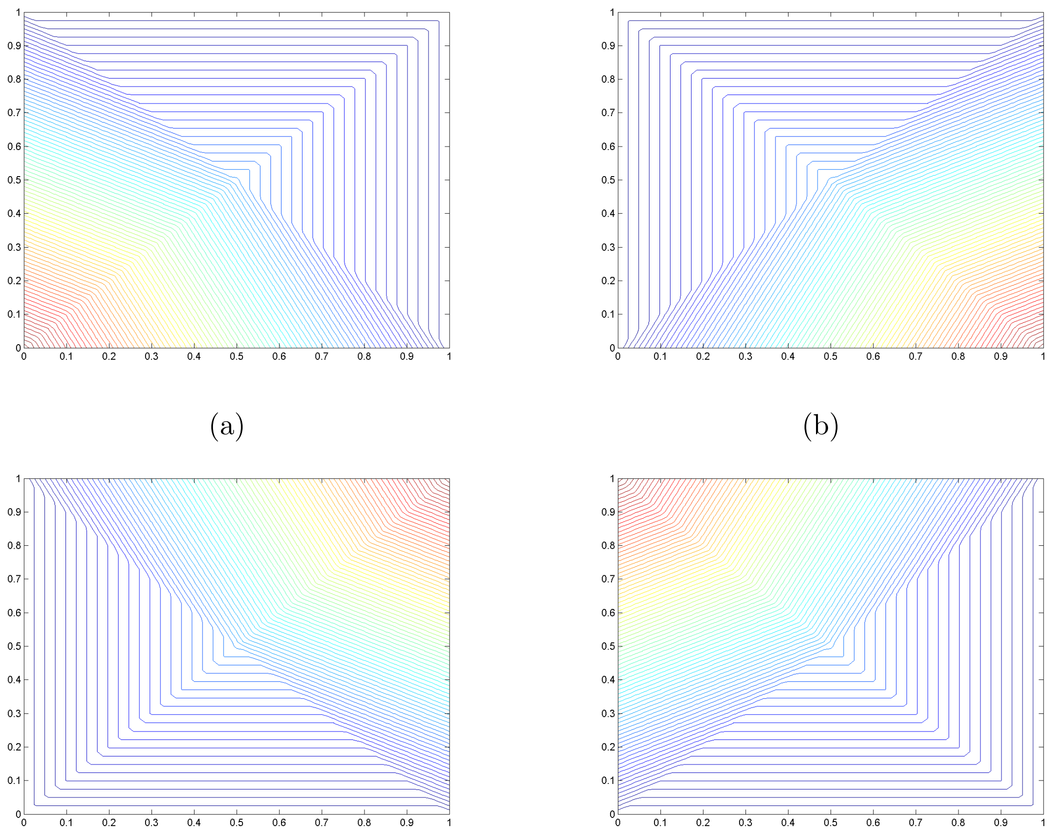

(a) (b) (c) (d)

Figure 3.2: Contour plots of the PWL basis functions on the unit square for the vertices located at: (a) (0,0), (b) (1,0), (c) (1,1), and (d) (0,1).

3.1.4 Mean Value Basis Functions

$$b_j^{MV}(\vec{x}) = \frac{w_j(\vec{x})}{\sum_i w_i(\vec{x})} \tag{3.11}$$

where the weight function for vertex j, w_j, has the following definition:

$$w_j(\vec{x}) = \frac{\tan(\alpha_{j-1}/2) + \tan(\alpha_j/2)}{|\vec{x}_j - \vec{x}|} \tag{3.12}$$

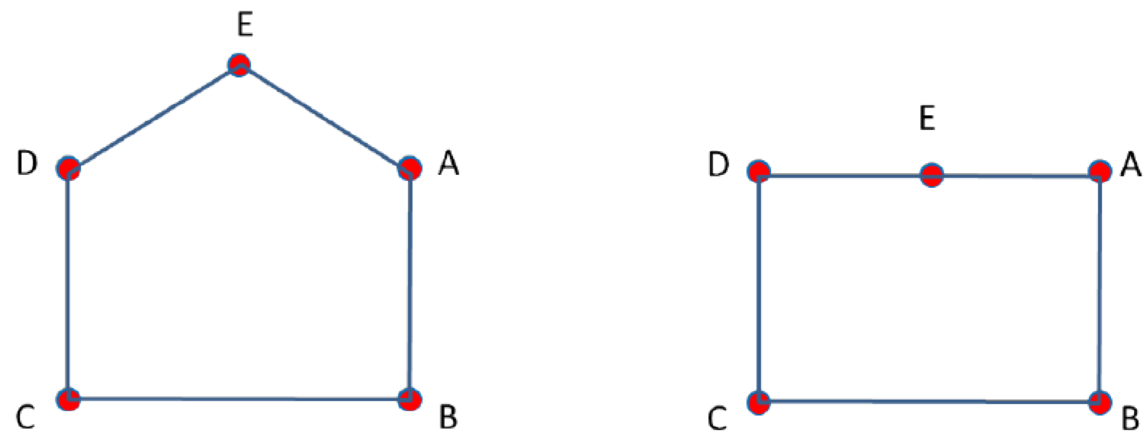

(a) (b)

Figure 3.3: Vertex structure for a (a) regular pentagonal cell and a (b) degenerate pentagonal cell.

3.1.5 Maximum Entropy Basis Functions

The final linearly-complete 2D basis functions that we will analyze in this work are generated by use of the *maximum entropy coordinates* (ME) [12, 13].

$$b_j^{ME}(\vec{x}) = \frac{w_j(\vec{x})}{\sum_i w_i(\vec{x})} \tag{3.13}$$

where the weight function for vertex j, w_j, has the following definition:

$$w_j(\vec{x}) = m_j(\vec{x}) \exp(-\kappa \cdot (\vec{x}_j - \vec{x})) \tag{3.14}$$

$$m_j(\vec{x}) = \frac{\pi_j(\vec{x})}{\sum_k \pi_k(\vec{x})} \tag{3.15}$$

where

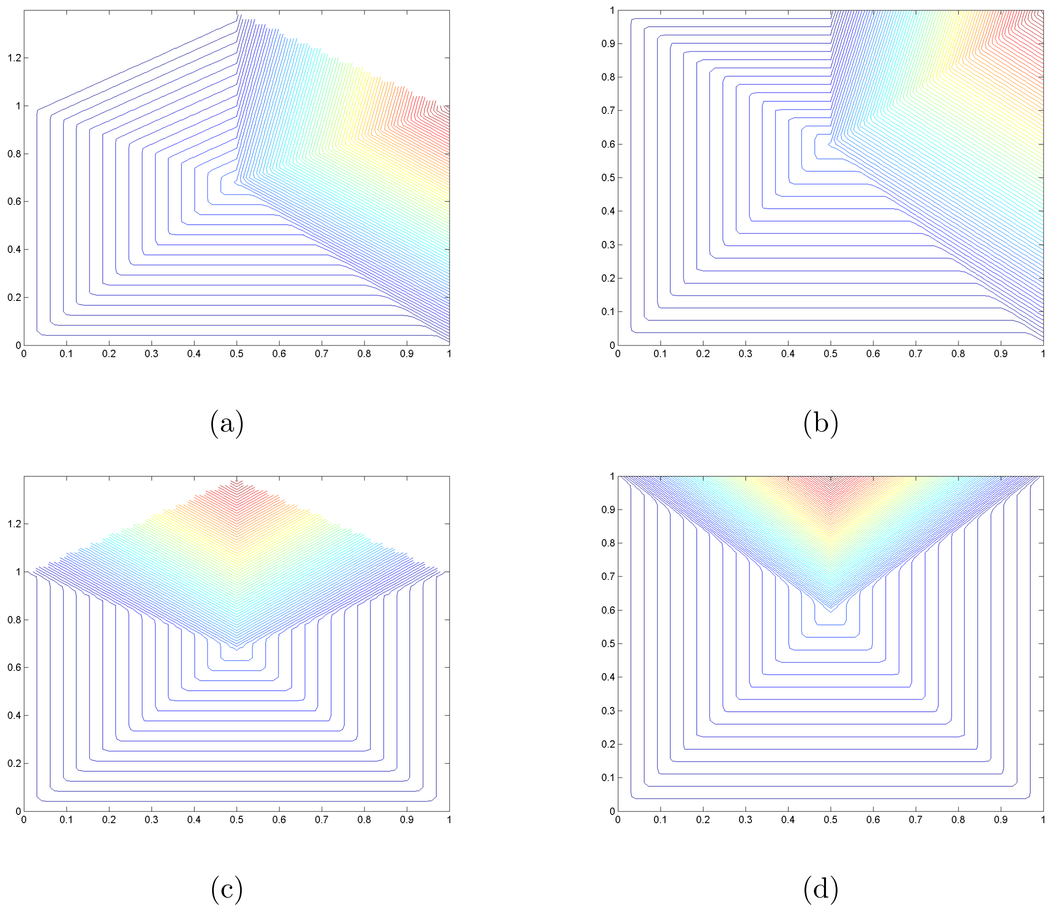

Figure 3.4: Contour plots of the PWL basis functions for a regular pentagon: (a) and (c) as well as a degenerate pentagon: (b) and (d).

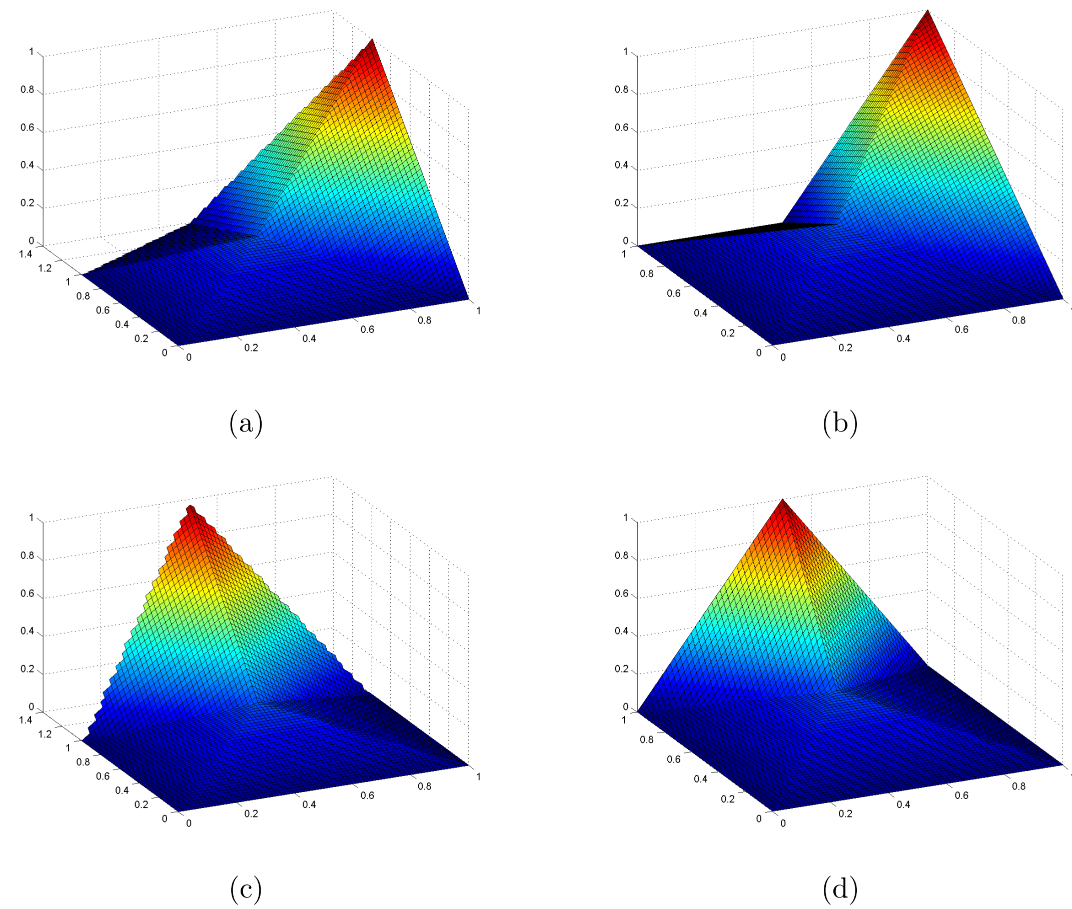

Figure 3.5: Plots of the PWL basis functions for a regular pentagon: (a) and (c) as well as a degenerate pentagon: (b) and (d).

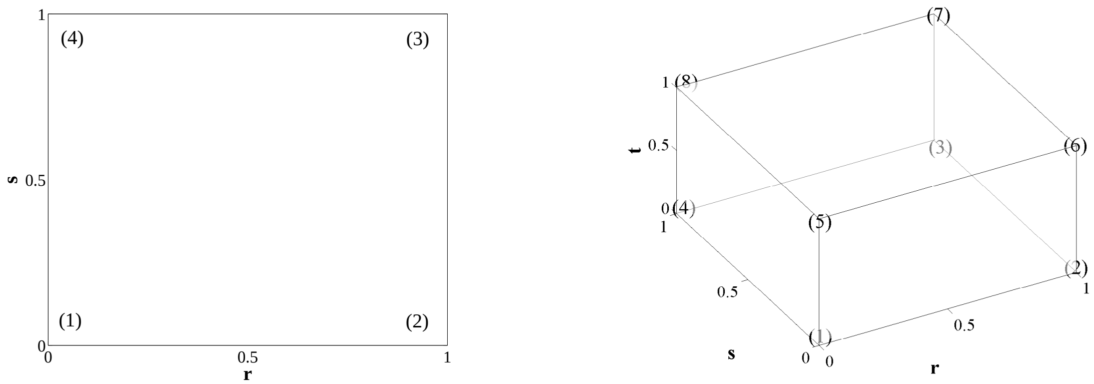

(a) (b)

Figure 3.6: Vertex structure for the (a) unit square and (b) unit cube.

$$\pi_j(\vec{x}) = \prod_{i \neq j-1,j} \rho_j(\vec{x}) \tag{3.16}$$

where

$$\rho_j(\vec{x}) = ||\vec{x} - \vec{x}_j|| + ||\vec{x} - \vec{x}_{j+1}|| - ||\vec{x}_{j+1} - \vec{x}_j|| \tag{3.17}$$

3.1.6 Summary of 2D Linear Basis Functions on Polygons

3.2 Quadratic Serendipity Basis Functions on 2D Polygons

3.2.1 Traditional Quadratic Basis Functions - $\mathbb{P}_2$ and $\mathbb{S}_2$ Spaces

3.2.2 Quadratic Mean Value Coordinates on 2D Polygons

3.2.3 Quadratic Maximum Entropy Coordinates on 2D Polygons

3.3 Linear Basis Functions on 3D Polyhedra

3.3.1 3D Linear and TriLinear Basis Functions

$$
\begin{aligned}
b_1(r,s) &= 1 - r - s - t \\
b_2(r,s) &= r \\
b_3(r,s) &= s \\
b_4(r,s) &= t
\end{aligned}
\tag{3.18}
$$

and

$$
\begin{aligned}
b_1(r,s,t) &= (1-r)(1-s)(1-t) \\
b_2(r,s,t) &= r(1-s)(1-t) \\
b_3(r,s,t) &= rs(1-t) \\
b_4(r,s,t) &= (1-r)s(1-t) \\
b_5(r,s,t) &= (1-r)(1-s)t \\
b_6(r,s,t) &= r(1-s)t \\
b_7(r,s,t) &= rst \\
b_8(r,s,t) &= (1-r)st
\end{aligned}
\tag{3.19}
$$

3.3.2 3D Piecewise Linear (PWL) Basis Functions

The 3D PWL basis functions share a similar form to the 2D PWL basis functions.

$$b_j(x,y,z) = t_j(x,y,z) + \sum_{f=1}^{F_j} \beta_f^j t_f(x,y,z) + \alpha_j^K t_c(x,y,z) \tag{3.20}$$

t_j is the standard 3D linear function with unity at vertex j that linearly decreases to zero to the cell center, the face center for each face that includes vertex j, and each vertex that shares an edge with vertex j. t_c is the 3D cell "tent" function which is unity at the cell center and linearly decreases to zero to each cell vertex and face center. t_f is the face "tent" function which is unity at the face center and linearly decreases to zero at each vertex on that face and the cell center. $\beta_{f,j}$ is the weight parameter for face f touching cell vertex j, and F_j is the number of faces touching vertex j. Like the previous work defining the PWLD method [14], we also choose to assume the cell and face weighting parameters are

$$\alpha_{K,j} = \frac{1}{N_K} \qquad \text{and} \qquad \beta_{f,j} = \frac{1}{N_f}, \tag{3.21}$$

respectively, where N_K is the number of vertices in cell K and N_f is the number of vertices on face f, which leads to constant values of α and β for each cell and face, respectively. This assumption of the cell weight function holds for both 2D and 3D.

3.4 Numerical Results

Now that we have presented several linear polygonal finite element basis sets along with the methodology to convert them to quadratic serendipity-like basis, we present several numerical problems to demonstrate our methodology. First, we demonstrate that the presented basis sets can capture an exactly-linear transport solution in Section 3.4.1. Next, we present some convergence properties of the basis sets using the method of manufactured solutions (MMS) in Section 3.4.2. We then present a searchlight problem and observe how the basis sets react with adaptive mesh refinement (AMR) to mitigate numerical dispersion through a vacuum in Section 3.4.3.

3.4.1 Two-Dimensional Exactly-Linear Transport Solutions

We present our first numerical example by demonstrating that the linear and quadratic polygonal finite element basis functions capture an exactly-linear solution space. We will show this by the method of exact solutions (MES). Since the coordinate interpolation of the basis functions for the linear basis functions requires exact linear interpolation (Eq. (3.2)), then an exactly-linear solution space can be captured, even on highly distorted polygonal meshes. This also applies to the quadratic serendipity space since it is formed by the product-wise pairings of the linear basis functions. We build our exact solution by investigating the 2D, 1 energy group transport problem with no scattering and an angle-dependent distributed source,

$$\mu \frac{\partial \Psi}{\partial x} + \eta \frac{\partial \Psi}{\partial y} + \sigma_t \Psi = Q(x, y, \mu, \eta), \tag{3.22}$$

where the streaming term was separated into the corresponding two-dimensional terms. We chose to drop the scattering term for this example so that the error arising from iteratively converging our solution would have no impact.

We then define an angular flux solution that is linear in both space and angle along with the corresponding 0th moment scalar flux ($\Phi_{0,0} \rightarrow \Phi$) solution:

$$\begin{aligned} \Psi(x, y, \mu, \eta) &= ax + by + c\mu + d\eta + e \\ \Phi(x, y) &= 2\pi \left(ax + by + e \right) \end{aligned} . \tag{3.23}$$

One can immediately notice that our 0th moment solution is not dependent on angle.

We arrive at this solution by enforcing our 2D angular quadrature set to have the following properties:

$$\sum_q w_q = 2\pi \qquad \text{and} \qquad \sum_q w_q \begin{bmatrix} \mu_q \\ \eta_q \end{bmatrix} = \begin{bmatrix} 0 \\ 0 \end{bmatrix}. \tag{3.24}$$

Our boundary conditions for all inflow boundaries are then uniquely determined by the angular flux solution of Eq. (3.23). Inserting the angular flux solution of Eq. (3.23) into Eq. (3.22), we obtain the distributed source that will produce our exactly-linear solution space:

$$Q(x, y, \mu, \eta) = a\mu + b\eta + \sigma_t \left(c\mu + d\eta\right) + \sigma_t \left(ax + by + e\right). \tag{3.25}$$

It is noted that the angular dependence of the source can be removed (which can ease the code development burden) if one sets

$$\begin{aligned} a &= -c\,\sigma_t, \\ b &= -d\,\sigma_t. \end{aligned} \tag{3.26}$$

For this example, we test the various 2D polygonal finite element basis functions on six different mesh types. These mesh types include triangular, quadrilateral, and polygonal meshes:

1. Orthogonal cartesian mesh formed by the intersection of 11 equally-spaced vertices in both the x and y dimensions. This forms a 10x10 array of quadrilateral mesh cells.

2. Ordered-triangular mesh formed by the bisection of the previous orthogonal cartesian mesh (forming 200 triangles all of the same size/shape).

3. Quadrilateral shestakov grid formed by the randomization of vertices based on a skewness parameter [15, 16]. With a certain range of this skewness parameter, highly distorted meshes can be generated.

4. Sinusoidal polygonal grid that is generated by the transformation of a uniform orthogonal grid based on a sinusoid functional. The transformed vertices are then converted into a polygonal grid by computing a bounded Voronoi diagram.

5. Kershaw's quadrilateral z-mesh [17]. This mesh is formed by taking an orthogonal quadrilateral grid and displacing certain interior vertices only in the y dimension.

6. A polygonal variant of the quadrilateral z-mesh. The polygonal grid is formed in a similar manner to the sinusoidal polygonal mesh with a Voronoi diagram.

We also wish that both the angular flux solution as well as the 0th moment solution are strictly positive everywhere. Therefore, we set the function parameters in Eq. (3.23) to $\sigma_t = a = c = d = e = 1.0$ and $b = 1.5$. We gave the solution the 40% tilt in space ($a \neq b$) so that it would not align with the triangular mesh. Using an S8 LS quadrature set, we ran all combinations of the polygonal basis functions and the mesh types. The linear solutions for the Wachspress, PWL, mean value, linear maximum entropy, and quadratic serendipity maximum entropy basis functions are presented in Figures 3.7, 3.8, 3.9, 3.10, and 3.11, respectively. We can see that for all the polygonal basis functions, an exact linear solution is captured as shown by the unbroken nature of the contour lines. This even holds on the highly distorted quadrilateral shestakov mesh.

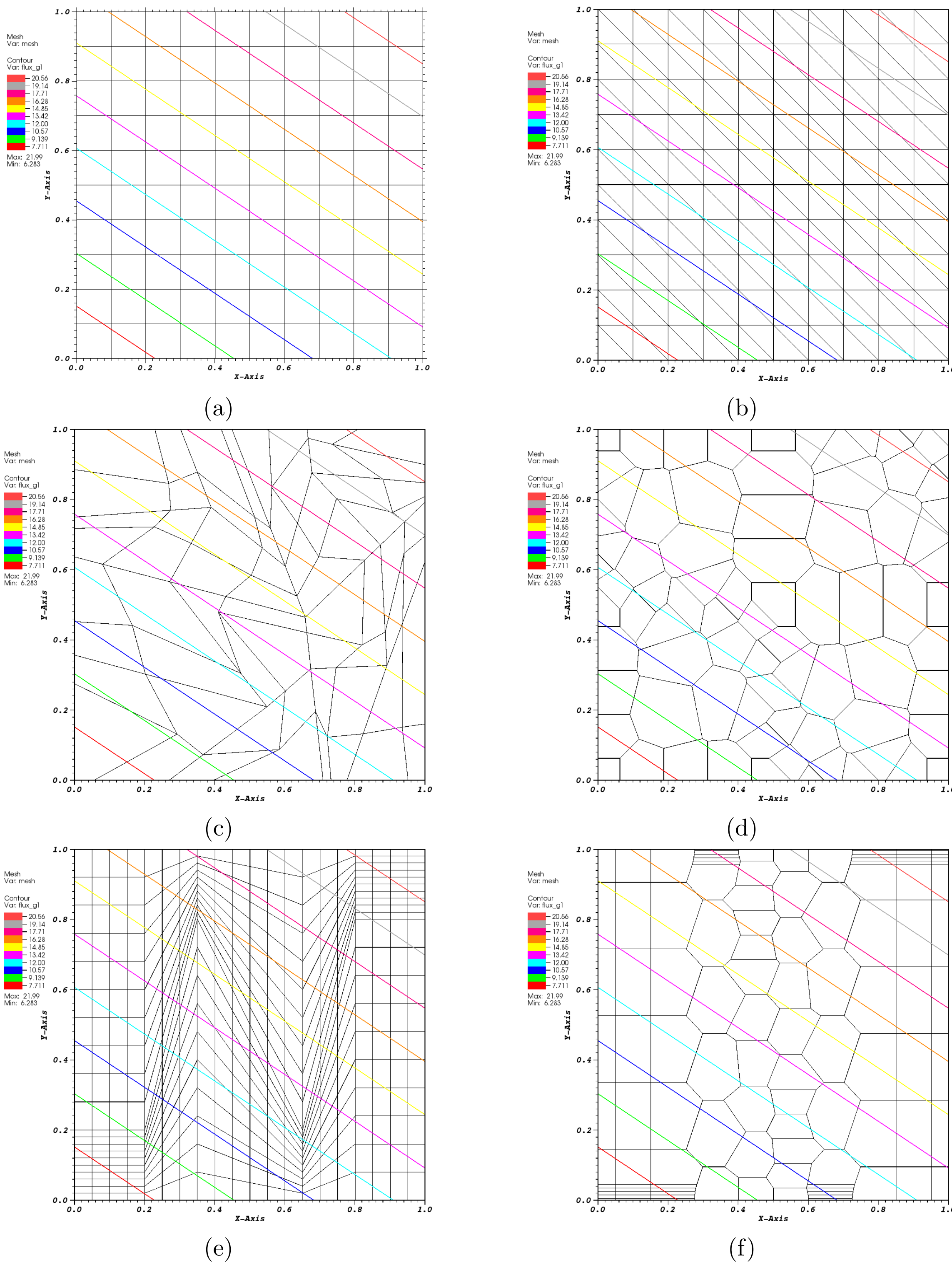

Figure 3.7: Contour plots of the exactly-linear solution with the Wachspress basis functions on (a) cartesian mesh, (b) ordered-triangular mesh, (c) quadrilateral shestakov mesh, (d) sinusoidal polygonal mesh, (e) quadrilateral z-mesh, and (f) polygonal z-mesh.

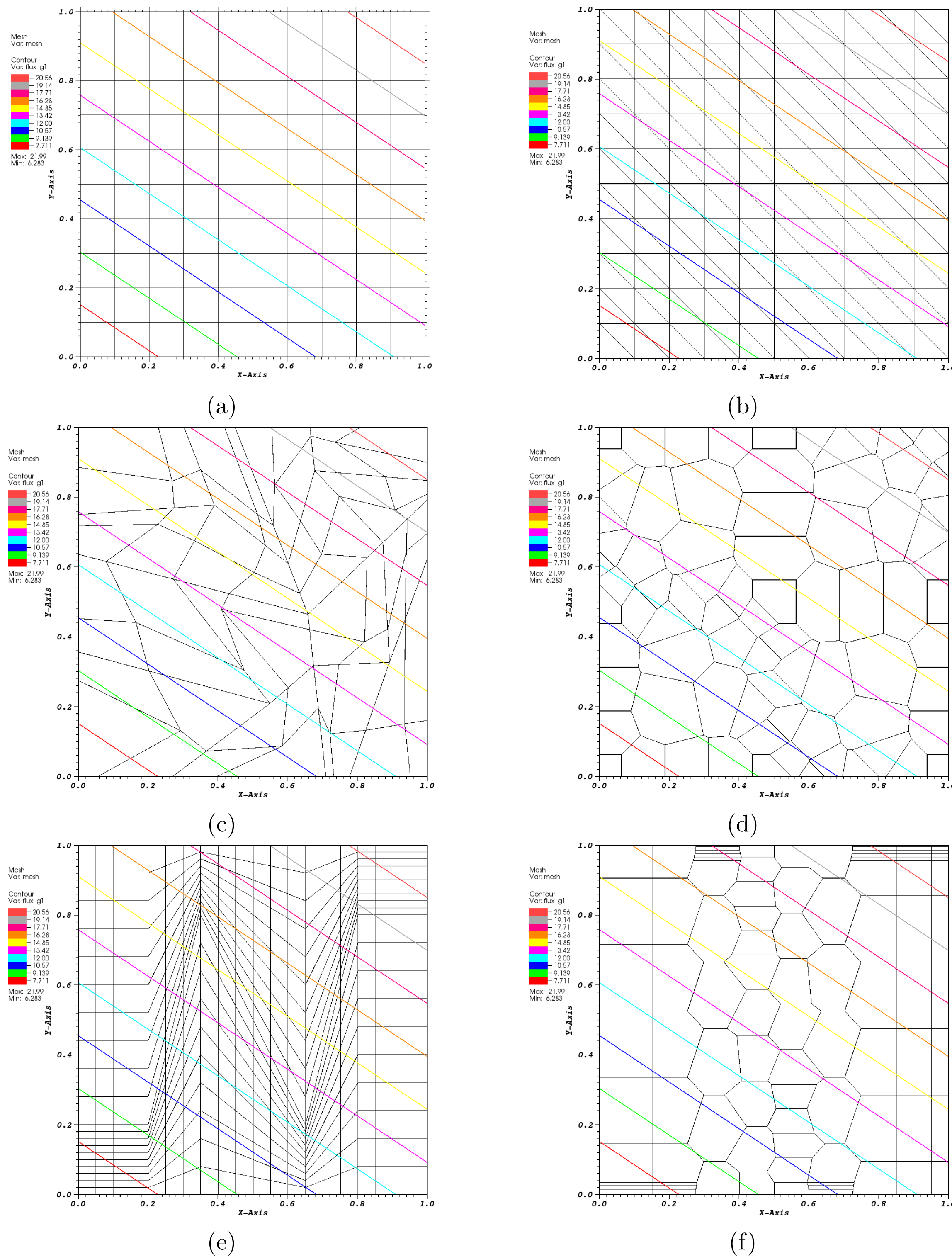

Figure 3.8: Contour plots of the exactly-linear solution with the PWL basis functions on (a) cartesian mesh, (b) ordered-triangular mesh, (c) quadrilateral shestakov mesh, (d) sinusoidal polygonal mesh, (e) quadrilateral z-mesh, and (f) polygonal z-mesh.

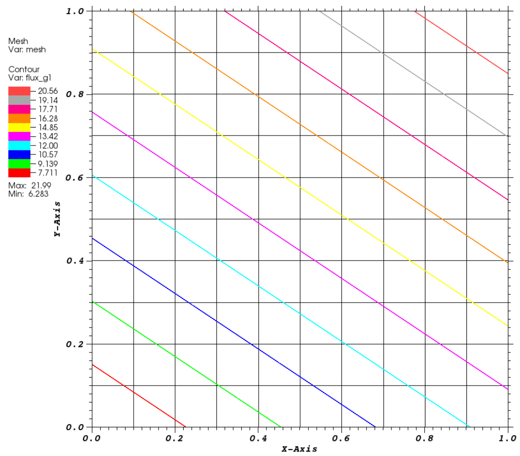

(a)

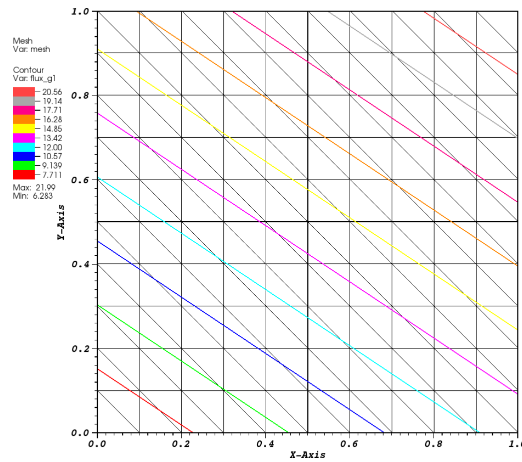

(b)

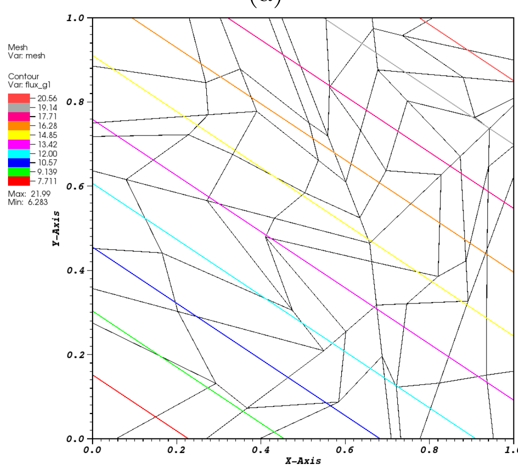

(c)

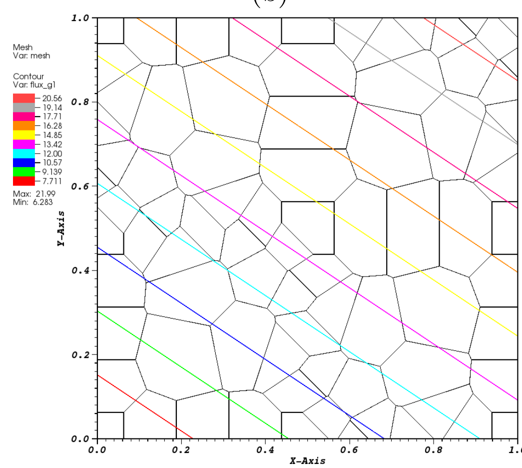

(d)

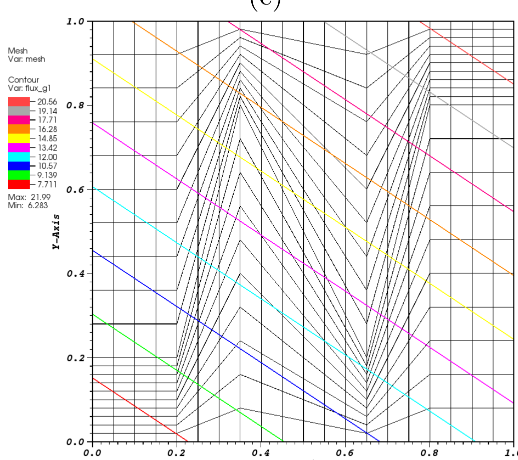

(e)

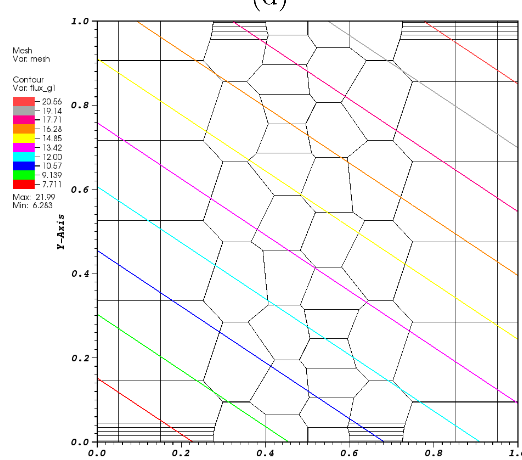

(f)

Figure 3.9: Contour plots of the exactly-linear solution with the mean value basis functions on (a) cartesian mesh, (b) ordered-triangular mesh, (c) quadrilateral shestakov mesh, (d) sinusoidal polygonal mesh, (e) quadrilateral z-mesh, and (f) polygonal z-mesh.

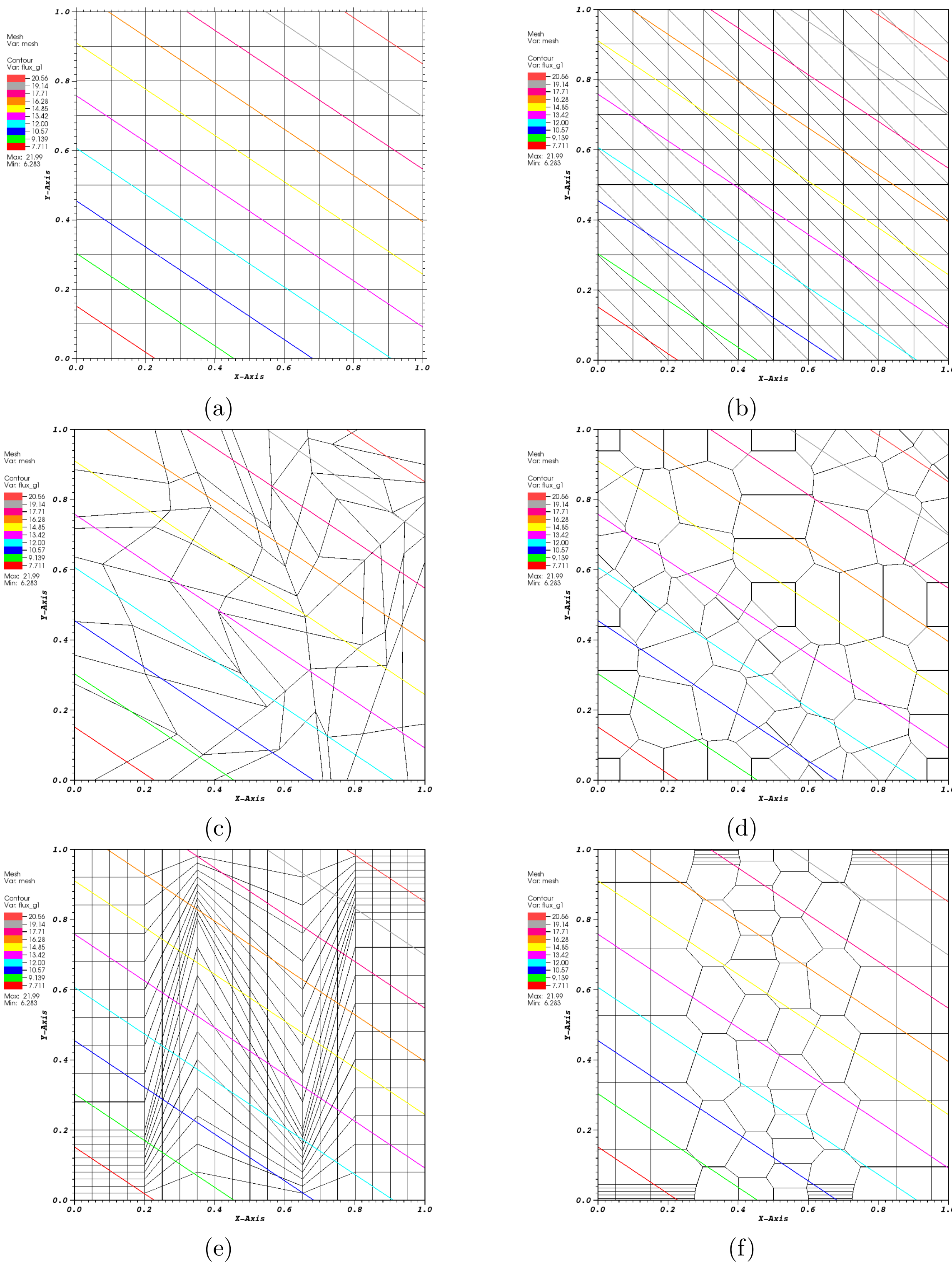

Figure 3.10: Contour plots of the exactly-linear solution with the linear maximum entropy basis functions on (a) cartesian mesh, (b) ordered-triangular mesh, (c) quadrilateral shestakov mesh, (d) sinusoidal polygonal mesh, (e) quadrilateral z-mesh, and (f) polygonal z-mesh.

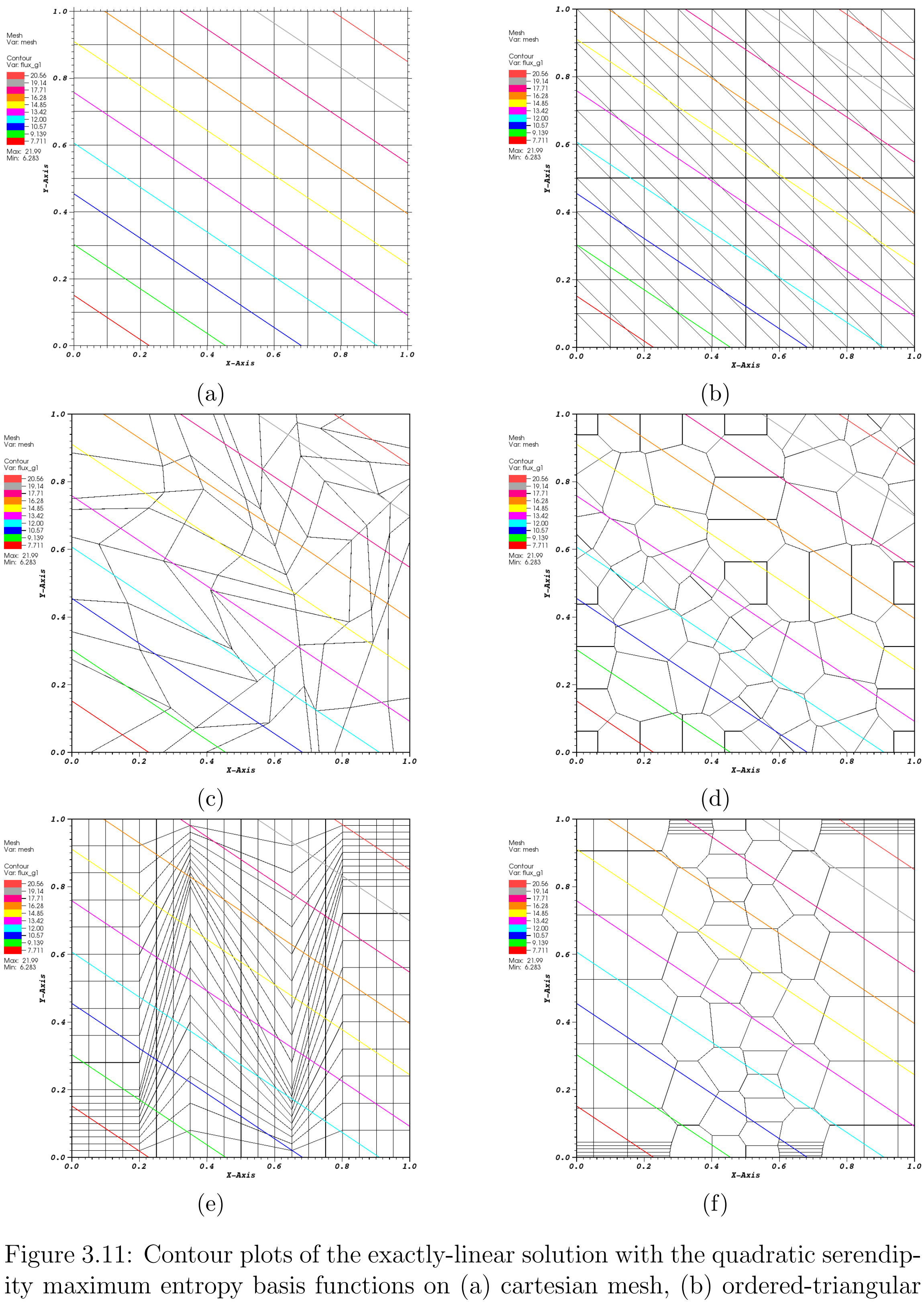

Figure 3.11: Contour plots of the exactly-linear solution with the quadratic serendipity maximum entropy basis functions on (a) cartesian mesh, (b) ordered-triangular mesh, (c) quadrilateral shestakov mesh, (d) sinusoidal polygonal mesh, (e) quadrilateral z-mesh, and (f) polygonal z-mesh.

3.4.2 Convergence Rate Analysis by the Method of Manufactured Solutions

The next numerical example we investigate involves calculating the convergence rate of the solution error via the method of manufactured solutions (MMS). Like MES, MMS enforces a given solution by use of a derived functional form for the driving source of the problem (Q_{ext}). However, unlike MES, we enforce a spatial solution that cannot be captured by the interpolation of the finite element space. Using a specification of the Bramble-Hilbert [18] lemma, the difference between the exact solution, Φ_e, and the discretized solution, Φ_h, residing in the Sobolev space, $W_{\mathcal{D}}^h \in \mathcal{T}_h$, for a given polynomial interpolation order, k, is

$$||\Phi_e - \Phi_h||_2 \leq C \frac{h^{q+1/2}}{(k+1)^q}, \tag{3.27}$$

where $q = \min(k + 1/2, r)$, h is the maximum diameter of all mesh cells, C is some constant independent of the mesh, r is a measure of the regularity of the transport solution, and $|| \cdot ||_2$ is the L_2 norm [19]. For transport solutions with sufficient discontinuities, r can approach 0. However, if the chosen solution is at least C^k continuous and a topologically regular mesh is used, then the convergence rate becomes strictly $(k+1)$. For structured meshes, h is straightforward to define. Unfortunately, this becomes a problem in general for polytope meshes. Instead, the grid resolution can be related to the number of spatial degrees of freedom (N_{dof}),

$$N_{dof} \propto h^{-d}, \tag{3.28}$$

where d is the dimensionality of the problem. Using this relationship for the grid resolution, along with the error norm of Eq. (3.27), we can define a general relationship between the error norm and the number of spatial degrees of freedom:

$$||\Phi_e - \Phi_h||_2 \propto N_{dof}^{-\frac{k+1}{d}}. \tag{3.29}$$

The result of Eq. (3.29) states that we expect convergence rates of N_{dof}^{-1} and $N_{dof}^{-2/3}$ for linear basis functions in 2D and 3D, respectively. Conversely, quadratic basis functions will yield convergence rates of $N_{dof}^{-3/2}$ and N_{dof}^{-1} in 2D and 3D, respectively.

For this example, we choose the following solution and problem parameters and characteristics:

1. Constant total cross section so that parameterized material properties are not necessary;
2. No scattering to avoid solution discontinuities from the S_N discretization;
3. No solution dependence in angle to avoid introducing angular discretization error;
4. Analytical solutions that are C^∞ continuous in space for both the angular flux and 0th order flux moment - this leads to integrable solution spaces that satisfy the Bramble-Hilbert lemma no matter what polynomial order is selected for the basis functions;
5. The angular flux solution is zero on the boundary for all incident directions - this is identical to vacuum boundaries which can ease code development.

To satisfy these characteristics, we choose to analyze two different solution spaces. The first is a smoothly varying sinusoid solution with no extreme local maxima. The second solution is a product of a quadratic function and a gaussian which yields a significant local maximum.

The sinusoid flux solutions, $\{\Psi^s,\, \Phi^s\}$, have the following parameterized form,

$$
\begin{aligned}
\Psi^s(x,y) =& \sin(\nu\frac{\pi x}{L_x})\sin(\nu\frac{\pi y}{L_y}),\\
\Phi^s(x,y) =& 2\pi\sin(\nu\frac{\pi x}{L_x})\sin(\nu\frac{\pi y}{L_y}),
\end{aligned}
\tag{3.30}
$$

where ν is a frequency parameter. We restrict this paremeter to positive integers ($\nu = 1, 2, 3, ...$) to maintain characteristic 5 of the solution and problem space. The gaussian solution space, $\{\Psi^g,\ \Phi^g\}$, that has its local maximum centered at (x_0, y_0) has the parameterized form,

$$
\begin{aligned}
\Psi^g(x,y) =& C_M x(L_x - x)y(L_y - y)\exp(-\frac{(x-x_0)^2 + (y-y_0)^2}{\gamma}),\\
\Phi^g(x,y) =& 2\pi C_M x(L_x - x)y(L_y - y)\exp(-\frac{(x-x_0)^2 + (y-y_0)^2}{\gamma}),
\end{aligned}
\tag{3.31}
$$

where the constants in the equations are:

$$
C_M = \frac{100}{L_x^2 L_y^2} \qquad \gamma = \frac{L_x L_y}{100}. \tag{3.32}
$$

For this example, we choose the dimensionality of our problem to be $[0,1]^2$ which makes $L_x = L_y = 1$ for both the sinusoid and gaussian solutions. For the sinusoid solution, we select the frequency parameter, ν, to be 3 and for the gaussian solution we set the local maximum: $x_0 = y_0 = 0.75$. With these parameters, the sinusoid solution will have local minima and maxima of -2π and 2π, respectively, and the gaussian solution will have a global maximum of $\frac{225}{32}\pi \approx 22.1$.

3.4.3 Searchlight Problem

The next example models a beam or searchlight. Similar problems were investigated in Dedner and Vollmöller [20] and Wang and Ragusa [21]. In this problem, an incident beam of neutrons is shined onto a small portion of a boundary, propagates

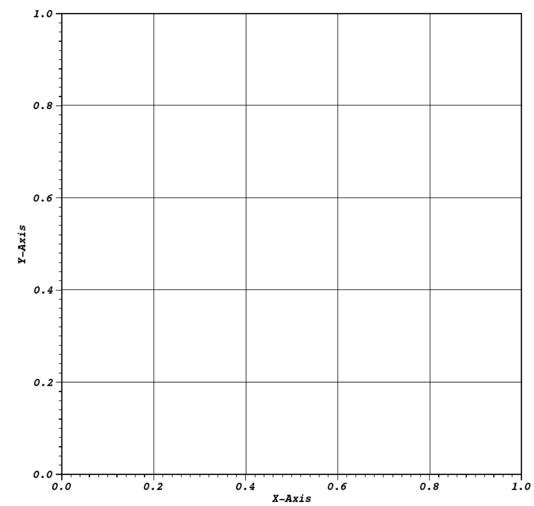

Figure 3.12: Initial mesh configuration for the searchlight problem before any refinement cycles.

through a vacuum, and then exits through a small portion of a different boundary. As the beam propagates through the vacuum, the spatial discretization causes radiation outflow through all downwind cell faces. This leads to numerical dispersion and will cause to beam to artificially broaden.

In this problem, we investigate an $\mathbb{R}^2$ domain of size $[0,1]^2$ cm. The radiation enters the left boundary between $0.2 \leq y \leq 0.4$ with an un-normalized angular direction of $[1, 0.4]$. For this chosen direction, the radiation beam would analytically leave the right boundary between $0.6 \leq y \leq 0.8$. This means that any radiation leaving the right boundary for all other y values is due to the numerical dispersion of the beam.

We investigated this problem using several of the 2D polygonal basis functions as outlined in Sections 3.1 and 3.2 as well as

3.5 Conclusions

In this chapter, we have presented

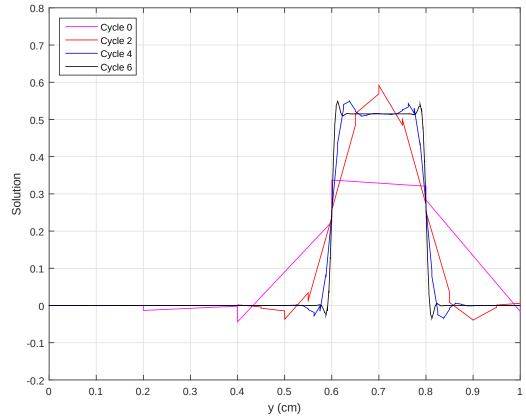

(a)

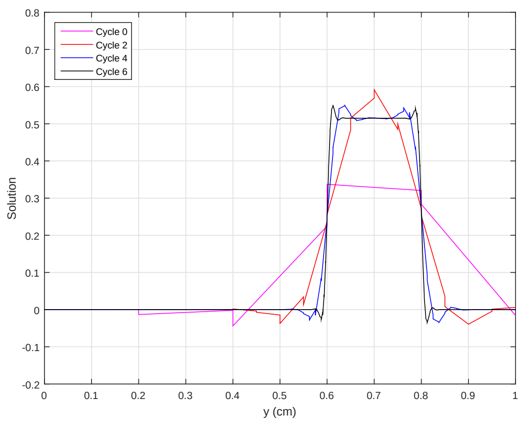

(b)

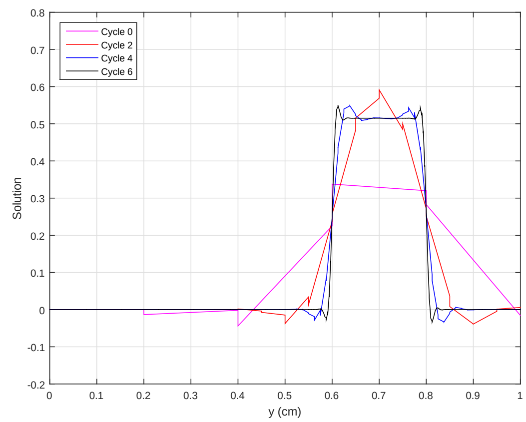

(c)

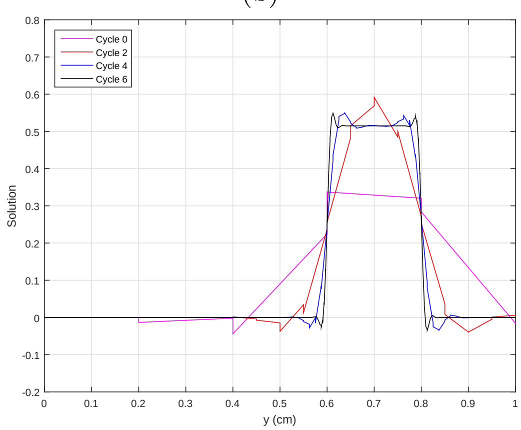

(d)

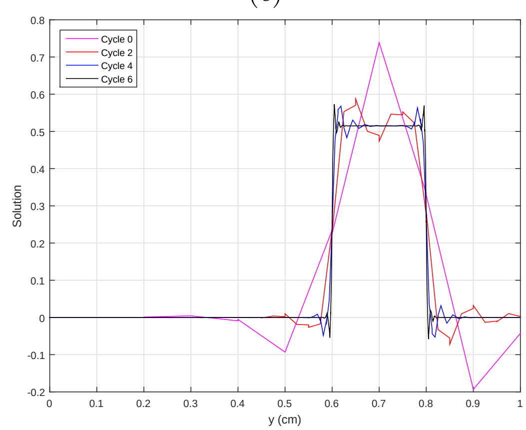

(e)

Figure 3.13: Exiting angular flux on the right boundary with uniform refinement using the (a) Wachspress basis functions, (b) PWL basis functions, (c) mean value basis functions, (d) linear maximum entropy coordinates and (e) quadratic serendipity maximum entropy coordinates.

REFERENCES

[1] R. LERNER and G. TRIGG, *Encyclopaedia of Physics*, 2 ed. (1991).

[2] C. PARKER, *McGraw Hill Encyclopaedia of Physics*, 2 ed. (1994).

[3] J. J. DUDERSTADT and W. R. MARTIN, *Transport theory*, John Wiley & Sons (1979).

[4] K. OTT and W. BEZELLA, *Introductory Nuclear Reactor Statics*, American Nuclear Society (1989).

[5] J. J. DUDERSTADT and L. J. HAMILTON, *Nuclear reactor analysis*, Wiley (1976).

[6] E. E. LEWIS and W. F. MILLER, *Computational methods of neutron transport*, John Wiley and Sons, Inc., New York, NY (1984).

[7] A. ERN and J.-L. GUERMOND, *Theory and practice of finite elements*, vol. 159, Springer Science & Business Media (2013).

[8] T. A. WAREING, J. M. MCGHEE, J. E. MOREL, and S. D. PAUTZ, "Discontinuous finite element S_N methods on three-dimensional unstructured grids," *Nuclear science and engineering*, **138**, *3*, 256–268 (2001).

[9] O. ZEINKIEWICZ, R. TAYLOR, and J. ZHU, *The finite element method: its basis and fundamentals*, SElsevier Butterworth-Heinemann (2005).

[10] J. AKIN, *Application and implementation of finite element methods*, Academic Press, Inc. (1982).

[11] R. J. ZERR, *Solution of the within-group multidimensional discrete ordinates transport equations on massively parallel architectures*, Ph.D. thesis, The Pennsylvania State University (2011).

[12] N. SUKUMAR, "Construction of polygonal interpolants: a maximum entropy approach," *International Journal for Numerical Methods in Engineering*, **61**, *12*, 2159–2181 (2004).

[13] K. HORMANN and N. SUKUMAR, "Maximum entropy coordinates for arbitrary polytopes," in "Computer Graphics Forum," Wiley Online Library (2008), vol. 27, pp. 1513–1520.

[14] T. S. BAILEY, *The piecewise linear discontinuous finite element method applied to the RZ and XYZ transport equations*, Ph.D. thesis, Texas A&M University (2008).

[15] A. SHESTAKOV, J. HARTE, and D. KERSHAW, "Solution of the diffusion equation by finite elements in lagrangian hydrodynamic codes," *Journal of Computational Physics*, **76**, *2*, 385–413 (1988).

[16] A. SHESTAKOV, D. KERSHAW, and G. ZIMMERMAN, "Test problems in radiative transfer calculations," *Nuclear science and engineering*, **105**, *1*, 88–104 (1990).

[17] D. S. KERSHAW, "Differencing of the diffusion equation in Lagrangian hydrodynamic codes," *Journal of Computational Physics*, **39**, *2*, 375–395 (1981).

[18] J. H. BRAMBLE and S. HILBERT, "Estimation of linear functionals on Sobolev spaces with application to Fourier transforms and spline interpolation," *SIAM Journal on Numerical Analysis*, **7**, *1*, 112–124 (1970).

[19] P. HOUSTON, C. SCHWAB, and E. SÜLI, "Stabilized hp-finite element methods for first-order hyperbolic problems," *SIAM Journal on Numerical Analysis*, **37**, *5*, 1618–1643 (2000).

[20] A. DEDNER and P. VOLLMÖLLER, "An adaptive higher order method for solving the radiation transport equation on unstructured grids," *Journal of Computational Physics*, **178**, *2*, 263–289 (2002).

[21] Y. WANG and J. C. RAGUSA, "Standard and goal-oriented adaptive mesh refinement applied to radiation transport on 2D unstructured triangular meshes," *Journal of Computational Physics*, **230**, *3*, 763–788 (2011).